ADVANCED FUNCTIONAL MATERIALS

Supporting Information

for *Adv. Funct. Mater.,* DOI: 10.1002/adfm.202111840

Unmasking the Resolution–Throughput Tradespace of Focused-Ion-Beam Machining

*Andrew C. Madison, John S. Villarrubia, Kuo-Tang Liao, Craig R. Copeland, Joshua Schumacher, Kerry Siebein, B. Robert Ilic, J. Alexander Liddle, and Samuel M. Stavis**

Supporting Information *for*
Unmasking the resolution–throughput tradespace of focused-ion-beam machining

Andrew C. Madison[1] John S. Villarrubia[1] Kuo-Tang Liao[1,2] Craig R. Copeland[1] Joshua Schumacher[3] Kerry Siebein[3] B. Robert Ilic[1,3] J. Alexander Liddle[1] and Samuel M. Stavis[1,*]

Index[4,5]

[1]Microsystems and Nanotechnology Division, National Institute of Standards and Technology, Gaithersburg, Maryland, USA. [2]Maryland Nanocenter, University of Maryland, College Park, Maryland, USA. [3]CNST NanoFab, National Institute of Standards and Technology, Gaithersburg, Maryland, USA. *e-mail: samuel.stavis@nist.gov. [4]We report uncertainties as 95% coverage intervals, or we note otherwise. [5]We fit models to data by damped least-squares with uniform weighting, or we note otherwise.

Note S1. Fabrication methods

We form a silica layer on substrates of p-type silicon with a crystallographic orientation of ⟨100⟩ by thermal oxidation in a furnace at atmospheric pressure, at a temperature of 1100 °C, with an oxygen flow rate of 1000 mL min^{-1} (1000 sccm) and a ratio of hydrogen to oxygen of 1.85. We sputter-deposit chromia, Cr_2O_3, of at least 99.8% purity on the silica layer, with a deposition power of 400 W, under argon at a pressure of 1.3×10^{-3} Pa (9.8×10^{-6} Torr), and with a deposition rate of 0.215 ± 0.005 nm s^{-1}, for 285 s.

We use an electron–ion beam system with a focused beam of gallium cations at an accelerating voltage of 30 kV, ion-beam currents ranging from 82 ± 1 pA to 796 ± 4 pA, which we measure prior to fabrication by deflecting the ion beam into a Faraday cup, a working distance between the final lens and the substrate surface of 4.2 mm, and normal incidence with respect to the sample (Table S2). Uncertainties of ion-beam currents are conservative estimates of 100% coverage intervals. We propagate uncertainties by Monte-Carlo methods.[1] We fit manufacturer specifications of the half-width at half-maximum of the focused ion beam as a function of ion-beam current to the power-law model in Equation (1).

We approximate the radius of our focused ion beam from the values of ion-beam current that we measure prior to fabrication (Table 11, Table S3). We use the radii from this power-law approximation to achieve an overlap of the ion beam of at least 50% between neighboring positions in the patterns.

For pattern control, we use text files with matrices that define lateral positions, dwell times, and Boolean parameters for beam deflection. We mill two test patterns. The first is a 10 by 10 array of points with dwell times that increase linearly across columns. We write this pattern in multiple passes ranging in total dwell time from 0.05 to 5 s to form approximately Gaussian pits (Table S2). The second test pattern resembles a darkening checkerboard, being a 20 by 20 array of adjacent squares of 1 by 1 μm, with ion doses that alternate between 0 pC μm^{-2} and a value that increases from 0 to approximately 1000 pC μm^{-2} across the columns and rows of the array in uniform increments of approximately 5 pC μm^{-2}. We choose this dose increment to target depth increments of 1 nm between adjacent squares in the checkerboard pattern on the basis of tests of the milling rate of silica.[2] We remove the sacrificial chromia mask by immersion in a mixture of nitric acid, ceric acid, and water with respective volumetric fractions of 6%, 16%, and 78% for 5 min.

We mill Fresnel lenses into silica coverslips with a thickness of approximately 170 μm, a root-mean-square surface roughness of less than 0.8 nm, and a surface quality with a scratch/dig specification of 20/10. We sputter-deposit a sacrificial mask of chromia with a thickness of 103 ± 2 nm onto a silica coverslip. We estimate the ion doses for radial profiles of Fresnel lenses from design depths and mean milling rates of chromia and silica (Note S10). We calculate the curvature of the lens design and trim the ion dose where the curvature drops below a critical value set by the inverse of the lateral extent of the ion beam (Note S11). We use the resulting radial profiles to interpolate values of ion dose for milling positions for each lens in a Cartesian coordinate system. We mill a single Fresnel lens directly into a silica coverslip with an ion-beam current of 26.3 ± 0.3 pA in a time of 3.75 h. We mill 75 Fresnel lenses in a square array through the sacrificial chromia mask and into silica with an ion-beam current of 2600 ± 30 pA in a time of 3.75 h. In this process, we aim to exhaust the mask, milling through its entire thickness to pattern each Fresnel lens and obviating the need for subsequent removal of the chromia by chemical etching.

Note S2. Characterization methods

We measure the thickness of the silica layer by ellipsometry. We measure the surface topography of the silica substrates before and after depositing the chromia mask. For all atomic force micrographs, we image regions of interest of approximately 25 by 25 μm with a line-scan resolution of 2048 points and at a rate of approximately 0.67 Hz. We use silicon-nitride cantilevers with a length of 27 μm, a resonant frequency of approximately 1400 kHz, a force constant of 17 N m^{-1}, and carrying a silicon tip with nominal front angle of 261 ± 44 mrad (15° ± 2.5°), a nominal back angle of 446 ± 44 mrad (25° ± 2.5°), a nominal radius of 5 nm, and a maximum radius of 12 nm. Assuming this geometry, the width of the probe is nominally 75 ± 7 nm at a depth of 100 nm, which is comparable to the smallest radii of test pits that we measure. Such a geometry imposes an upper limit on the aspect ratio of features that we expect to measure accurately. We input these manufacturer specifications of the probe tip geometry into a certainty-map algorithm to identify and ignore data in atomic force micrographs that exhibit artifacts from tip convolution.[3] We estimate uncertainties of atomic force microscopy by a combination of manufacturer specifications and previous tests (Table S3).[2]

We perform scanning electron microscopy with an acceleration voltage of 5 kV, a nominal electron-beam current of 100 pA, a working distance of 4.2 mm, and at normal incidence with respect to the microscope stage. In all scanning electron micrographs, the imaging mode is of secondary electrons incident on a through-lens detector. Before ion exposure, we record scanning electron micrographs of the chromia mask at a magnification of 250000× ± 7500×, which corresponds to a horizontal field width of 597 ± 18 nm. This uncertainty is a 100% coverage interval per the microscope specification.

We prepare a cross section of the chromia and silica layers for transmission electron microscopy by *ex situ* lift-out.[4] The dimensions of the cross section are approximately 10 μm in length, 5 μm in width, and 100 nm in depth. We image the cross section by brightfield transmission electron microscopy at an acceleration voltage of 300 kV.

We determine the solid-state of chromia by X-ray diffraction from 0.35 to 1.40 rad in increments of 0.1 mrad with a total reflection critical angle of 7.0 mrad. The incident X-rays correspond to copper Kα transitions, which have an energy of 1.29 fJ (8.04 keV) and a wavelength of 0.1506 nm. We fit an X-ray reflectivity model[5] to the resulting data to measure density, surface roughness, and thickness. We fit all models to data by damped least-squares estimation with uniform weighting. We estimate the sizes of crystallites present in X-ray diffractometry data using the Scherrer equation.

For in-line resolution metrology, we measure pits by scanning electron microscopy at a magnification of 5000× ± 150×, which corresponds to a horizontal field width of 29.8 ± 0.9 μm. We measure the surface topography of

complex nanostructures that we mill through chromia and into silica by atomic force microscopy before and after removal of the sacrificial mask.

We record brightfield micrographs of Fresnel lenses to characterize the projection distances and apparent sizes of focal spots from each lens through a focal volume of approximately 258 by 258 µm by 40 µm. We axially section the focal volume into 1001 micrographs, scanning vertically in increments of 40 ± 10 nm. For these micrographs, a light-emitting diode trans-illuminates the samples with a wavelength range from 420 to 510 nm. An objective lens with a nominal magnification of 50× and a numerical aperture of 0.95 collects transmission through air immersion. A tube lens projects the images onto a complementary metal–oxide–semiconductor (CMOS) camera with 2048 by 2048 pixels, each with an on-chip size of 6.5 by 6.5 µm. A mean factor of 2.0, per the specification of the camera manufacturer, converts from photoelectrons to analog-to-digital units. We operate the camera at a sensor temperature of -10 °C by thermoelectric and water cooling, without on-board correction of pixel noise, and in fast-scan mode, and we calibrate the imaging system for these parameters.

We calibrate the imaging system with an aperture array that has a pitch of 5001.45 ± 1.08 nm, determining a mean pixel size of 126.82 ± 0.03 nm.[6] We determine positions of best focus of lens surfaces by finding local maxima of a ninth-order polynomial model of image contrast in a range of images that we identify by inspection to include the top surface of the central zones of the lenses. We determine positions of best focus of images of focal spots by fitting symmetric Gaussian models to image data and minimizing a ninth-order polynomial model that we fit to the resulting standard deviations in a range of images that we identify by inspection. We determine projection distance as the difference between the two positions of best focus.

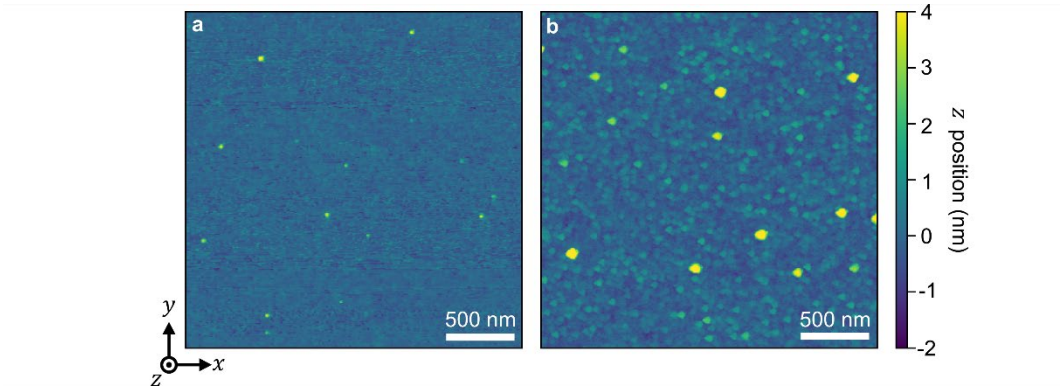

Figure S1. Silica and chromia. Atomic force micrographs showing a) silica before deposition of chromia and b) chromia before ion exposure. Comparison of the micrographs indicates that the areal densities of silica asperities and chromia patches with lateral dimensions exceeding 50 nm are comparable, as well as a convolution artifact of the probe tip in (b).

Table S1. Material properties

Material	Composition	Function	Measurement method	Density (g cm^{-3})	Thickness (nm) or (µm)	Root-mean-square roughness (nm)
Chromia	Cr_2O_3	Sacrificial mask	Atomic force microscopy	–	–	0.6 ± 0.2
			Transmission electron microscopy	–	63 ± 2 nm	–
			X-ray diffraction	5.3 ± 0.1	65 ± 3 nm	1.5 ± 0.4
Silica	SiO_2	Working material	Atomic force microscopy	–	–	0.3 ± 0.2
			X-ray diffraction	2.2 ± 0.1	488 ± 2 nm	0.4 ± 0.4
Silicon	Si	Substrate	Atomic force microscopy	–	–	0.3 ± 0.2
			Manufacturer specification	2.3	525 ± 25 µm	–

Uncertainties of density, thickness, and roughness by X-ray diffraction are conservative estimates of 100% coverage intervals.

Table S2. Milling parameters

Ion-beam current (pA)	Feature	Elements in array	Lateral extent of array (µm by µm)	Pitch of milling positions (nm)	Number of milling positions	Dwell time (µs)	Number of passes	Total milling time (s)
82 ± 1	pits	10 by 10	18 by 18	12.3	100	100	3052	275.2
219 ± 2	pits	10 by 10	18 by 18	19.8	100	100	1526	137.6
407 ± 2	pits	10 by 10	18 by 18	26.8	100	100	611	55.0
773 ± 3	pits	10 by 10	18 by 18	36.7	100	100	306	27.5
83 ± 1	squares	20 by 20	20 by 20	12.4	1312200	100	59	1241.9
227 ± 1	squares	20 by 20	20 by 20	20.2	472424	100	14	434.2
421 ± 3	squares	20 by 20	20 by 20	27.3	253504	100	22	228.9
796 ± 4	squares	20 by 20	20 by 20	37.2	133136	100	56	118.6
26 ± 0.3	lenses	1 by 1	15 by 15	7.0	3414413	50	155	13500
2600 ± 30	lenses	7.5 by 10	150 by 120	66.4	2791725	50	166	13500
2600 ± 30	lenses	1 by 1	15 by 15	66.4	36473	50	143	144

Uncertainties of ion-beam current are conservative estimates of 100% coverage intervals.
The milling time of pits includes a 0.4 µs pause to unblank and blank the ion beam before and after milling at each beam position.

Table S3. Statistical variables

Variable	Type of variable	Symbol	Distribution	Type[7] of evaluation	Value	Units
Localization uncertainty in SEM micrographs	Uncertainty	$u_{\text{loc, SEM}}$	Normal	B	Mean: $s_{0,\text{SEM}}$, SD: $\sigma_{\text{loc, SEM}}$	nm
Localization uncertainty in AFM micrographs	Uncertainty	$u_{\text{loc, AFM}}$	Normal	B	Mean: $s_{0,\text{AFM}}$, SD: $\sigma_{\text{loc, AFM}}$	nm
Standard deviation of Gaussian filter	Dimension	σ_{G}	Uniform	A	Range: 10 to 30	nm
Window length of Savitzky-Golay filter	Dimension	ω_{SG}	Uniform	A	Range: 13 to 27, odd values	pixels
Secondary electron scattering intensity	Dimension	I_{SE}	Normal	B	Mean: $I_{\text{SE}}(s(\theta))$, SD: σ_{SE}	arb.
Magnification uncertainty in SEM micrographs	Uncertainty	u_{mag}	Uniform	B	Range: -0.03a_{SEM} to 0.03a_{SEM}	–
Mean pixel size of SEM micrographs	Dimension	a_{SEM}	Delta	A	4.9	nm
Calibration errors of atomic force microscope	Uncertainty	u_{cal}	Normal	A	Mean: 0, SD: $0.0025 \cdot z$	nm
Position errors from surface roughness	Uncertainty	u_{rough}	Normal	A	Mean: 0, SD: 0.030	nm
Position errors from flatness	Uncertainty	u_{flat}	Normal	A	Mean: 0, SD: 0.065	nm
Position uncertainty due to AFM probe tip	Dimension	u_{tip}	Uniform	B	Range: -0.5· r_{tip} to 0.5· r_{tip}	nm
Maximum nominal radius of AFM probe tip	Dimension	r_{tip}	Delta	A	5	nm
Radius of pits in SEM micrographs	Dimension	$r_{\text{p, SEM}}$	Empirical	B	$u_{\text{loc, SEM}}$, ω_{SG}, σ_{G}, I_{SE}, u_{mag}	nm
Radius of pits in AFM micrographs	Dimension	$r_{\text{p, AFM}}$	Empirical	B	$u_{\text{loc, AFM}}$, ω_{SG}, σ_{G}, u_{cal}, u_{rough}, u_{flat}, u_{tip}	nm
X-ray diffraction intensity	Dimension	I_{XRD}	Normal	B	Mean: I_{XRD}, SD: σ_{XRD}	arb.
Chromia density	Dimension	ρ_{m}	Normal	A	Mean: 5.3, SD: 0.05	g cm^{-3}
Silica density	Dimension	ρ_{s}	Normal	A	Mean: 2.2, SD: 0.05	g cm^{-3}
Root-mean-square roughness of chromia	Dimension	$R_{\text{q, m}}$	Normal	A	Mean: 1.5, SD: 0.4	nm
Root-mean-square roughness of silica	Dimension	$R_{\text{q, s}}$	Normal	A	Mean: 0.4, SD: 0.2	nm
Depth of features in AFM micrographs	Dimension	z_s	Empirical	B	u_{cal}, u_{rough}, u_{flat}, u_{tip}	nm
Chromia thickness	Dimension	z_{m}	Normal	A	Mean: 63, SD: 1	nm
Milling rates of chromia on silica	Dimension	m_i	Normal	B	Table S6	µm^3 nA^{-1} s^{-1}
Intercepts of milling responses	Dimension	b_i	Normal	B	Table S6	nm
Mean milling rate of chromia	Dimension	$\bar{m}_{\text{m}}$	Normal	B	Mean: 0.15, SD: 0.02	µm^3 nA^{-1} s^{-1}
Mean milling rate of silica	Dimension	$\bar{m}_{\text{s}}$	Normal	B	Mean: 0.24, SD: 0.02	µm^3 nA^{-1} s^{-1}
Ion-beam current	Dimension	I	Normal	A	Table S2	pA
Coefficient of power law of ion-beam HWHM	Dimension	α_{beam}	Normal	B	Mean: 1.43, SE: 0.12	nm pA$^{-\beta}$
Exponent of power law of ion-beam HWHM	Dimension	β_{beam}	Normal	B	Mean: 0.49, SE: 0.01	–
Coefficient of power law of width of step edges	Dimension	α	Normal	B	Mean: 60, SD: 13	nm pA$^{-\beta}$
Exponent of power law of width of step edges	Dimension	β	Normal	B	Mean: 0.20, SD: 0.05	–
Widths of edges before chromia removal	Dimension	w_{b}	Empirical	B	u_{cal}, u_{rough}, u_{flat}, u_{tip}	nm
Widths of edges after chromia removal	Dimension	w_{a}	Empirical	B	u_{cal}, u_{rough}, u_{flat}, u_{tip}	nm
Effective lateral resolution or super-resolution	Dimension	$\mathcal{R}$	Empirical	B	α, β, $\mathcal{F}_{\text{SR}}$	nm
Super-resolution factor	Dimension	$\mathcal{F}_{\text{SR}}$	Empirical	B	u_{cal}, u_{rough}, u_{flat}, u_{tip}	–
Physical selectivity of chromia and silica	Dimension	$\mathcal{S}$	Empirical	B	u_{cal}, u_{rough}, u_{flat}, u_{tip}	–
Temporal efficiency	Dimension	η_τ	Empirical	B	u_{cal}, u_{rough}, u_{flat}, u_{tip}	–
Temporally efficient milling range	Dimension	ζ_{max}	Empirical	B	u_{cal}, u_{rough}, u_{flat}, u_{tip}, β	–
Volume throughput	Dimension	$\mathcal{V}$	Empirical	B	u_{cal}, u_{rough}, u_{flat}, u_{tip}, $\bar{m}_{\text{m}}$, $\bar{m}_{\text{s}}$, i	µm^3 hr^{-1}
Figure of merit of focused-ion-beam milling	Dimension	$\mathcal{M}$	Empirical	B	$\mathcal{R}$, $\mathcal{V}$	µm^2 hr^{-1}

SEM = scanning electron microscopy
SD = standard deviation
AFM = atomic force microscopy
HWHM = half width at half maximum
SE = standard error
We treat the bulk milling rate of silica as its mean value.
We extend the conventional evaluation Type from uncertainties to dimensions.

Note S3. Image formation

We observe a near equality of test-pit radii corresponding to the maximum signals of secondary electrons in scanning electron micrographs and the maximum convexity of surface profiles in atomic force micrographs. Secondary electrons from test pits form images with two main features of dark centers within bright rings, both of which are within the outer rims of the test pits (Figure 3c). In a previous study,[8] similar signals resulted from test pits in silicon ⟨111⟩ and glassy carbon. However, the authors of this previous study removed the bright rings by a threshold and approximated the dark central features with a symmetric bivariate Gaussian function. This approximation would be inaccurate for our scanning electron micrographs and would lead to errors in measurements of pit radius. To better understand the empirical correlation that we use for in-line resolution metrology, we investigate the influence of the surface topography on the theoretical signal of secondary electrons, using fundamental concepts of image formation in scanning electron microscopy. A symmetric bivariate Gaussian surface, which has deviations in z position of approximately 5% in comparison to the surface profiles of our test pits (Figure 3c), is a reasonable approximation of our pit topography for theoretical analysis. Our calculations lead to a new interpretation of the image data.

We expect three effects to dominate image contrast in scanning electron micrographs of pits. First, tilt contrast results from the dependence of the secondary-electron yield on the tilt angle, ϕ, of the local surface-normal relative to the incident electron-beam. The secant of the tilt angle, $\sec\phi$, is a common approximation of secondary-electron emission due to surface topography.[9] Second, shadow contrast results from surfaces of the pit that reabsorb secondary electrons, obscuring access to the top surface of the sample where an extraction bias pulls electrons toward the detector, reducing signals that originate within the basin of the pit.[4, 9b, 10] Third, material contrast results from local variations in secondary-electron yield due to the presence of the chromia–silica bilayer, gallium dopants from the ion beam, and redeposition during sputtering, further modulating the superimposition of tilt and shadow effects. Although diffusion effects are also relevant, we expect a diffusion length of order 10^0 nm for secondary electrons in our system. Additionally, we expect the diffusion effect to contribute more to image formation for surface regions of higher slope than for surface regions of lower slope. Therefore, we expect that our analysis of tilt contrast captures relevant spatial information from the diffusion effect.

To investigate the effects of pit topography on image formation, we compute tilt and shadow contrast for images of the surface of a Gaussian pit, $S(x, y)$, with an aspect ratio that is comparable to that of the test pits. With diameters ranging from approximately 160 to 360 nm and corresponding depths ranging from approximately 30 to 100 nm, the aspect ratios of test pits vary from approximately 0.2 to 0.3. For a path along the x direction and through the center of the Gaussian pit, we calculate the primary signal, $\sec\phi = \sqrt{1 + (\partial S/\partial x)^2}$, resulting from tilt contrast. For simplicity, we exploit the axial symmetry of the pit and the orientation of the path of interest in the x direction to ignore the y component of the surface in our calculation of the primary signal. We model shadow effects by calculating the accessibility of the surface of the pit to the zero plane, which corresponds to the flat surface above the pit. For any point on the zero plane, the accessibility is the solid angle that a hemisphere subtends, 2π sr, as any secondary electron escaping the surface is free to move toward a detector above the surface. The concavity of the surface of a Gaussian pit reduces the accessibility from a maximum value of 2π sr far from the center of the pit to a minimum value at the center of the pit (Figure S2a).

During imaging, an extraction field of approximately 17 kV m^{-1} pulls electrons toward an in-lens detector. However, the extraction field changes the electron energy by less than 1 part in 1000, so that straight lines are good approximations of electron trajectories within submicrometer test pits. This suggests that accessibility approximates shadow contrast from the surface of such pits. We calculate the accessibility, $\mathcal{A}(S, \boldsymbol{x}_i)$, of the i^{th} point on a path through the center of S in three dimensions by integrating the intervisibility function over the solid angle that the hemisphere subtends, Ω, in equation (S1),

$$\mathcal{A}(S, \boldsymbol{x}_i) = \frac{1}{\pi}\int_{\Omega} v\big(S, \boldsymbol{x}_i, \boldsymbol{r}(\omega)\big)d\omega\,, \tag{S1}$$

where the intervisibility,[11] $v(S, \boldsymbol{r}(\omega), \boldsymbol{x}_i)$, is either one or zero if S occludes a ray, $\boldsymbol{r}(\omega)$, emanating from a point on the surface profile, $\boldsymbol{x}_i = (x_i, y_i, z_i)$, in direction $\omega = (\theta, \varphi)$, where θ is the polar angle and φ is the azimuthal angle. We compute the intervisibility as

$$v(S, \boldsymbol{r}(\omega), \boldsymbol{x}_i) = 0\begin{cases}1, z_r > z_i + \dfrac{\|\boldsymbol{r}(\omega)\|}{\|\boldsymbol{x}_k - \boldsymbol{x}_i\|}(z_k - z_i) \text{ for all } \boldsymbol{x}_k \\ 0, \text{otherwise}\end{cases}, \tag{S2}$$

where $\boldsymbol{x}_k = (x_k, y_k, z_k)$ are intermediate points on the surface of the pit between $\boldsymbol{x}_i$ and the projection of $\boldsymbol{r}(\omega)$ onto the surface, z_r is the z position of the terminus of $\boldsymbol{r}(\omega)$. We use Monte-Carlo integration to compute Equation (S1) along $\boldsymbol{x}_i$. We set the length of $\boldsymbol{r}(\omega)$ to span the computational domain and achieve uniform sampling of ω over Ω in 10^5 random directions by $\theta = \cos^{-1}\big(\mathcal{U}(0,1)\big)$ and $\varphi = 2\pi\mathcal{U}(0,1)$, where $\mathcal{U}(0,1)$ represents a uniform distribution of with lower bound of zero and an upper bound of one. Lastly, we calculate the second spatial derivative of S and a factor of the signal intensity resulting from topographic contrast, $I_{\text{topography}}$, as the product of the surface-tilt and shadowing effects,

$$I_{\text{topography}} \propto \frac{\mathcal{A}(S, \boldsymbol{x}_i)}{2\pi} \sec\phi \,. \tag{S3}$$

Several results of this new analysis indicate a limit of tilt and shadow contrast to predict rings of high intensity in secondary electron images of Gaussian pits. First, the primary signals from tilt contrast appear as peaks in signal intensity at positions where the first spatial derivative, rather than the second spatial derivative, of S are maximal (Figure S2b). Next, the accessibility of S exhibits a concave structure, transitioning from maximum values of 2π sr outside of the pit to a minimum value of approximately π sr in the center of the pit (Figure S2c). In comparison, the negative of the second spatial derivative of S shows two maxima, each of which indicates positions of maximum convexity of S, and a global minimum in the center of the pit, indicating a position of maximum concavity (Figure S2d). We interpret these positions of maximum convexity as possible locations for material contrast to arise due to the implantation of gallium, interspersing of chromia and silica, and redeposition of the various materials on the surface of the pit. Last, the product of the tilt and shadow effects predicts a complex response that rises slowly near the outer rim of the pit and falls to a global minimum in the center of the pit (Figure S2e). The discrepancies between the product of tilt and shadow contrast, and the negative second derivative of S, also suggest that material contrast affects the formation of images of Gaussian pits. Further study is necessary to fully understand the cause of the empirical correlation of electron signals and pit curvature, which nonetheless enables in-line resolution metrology.

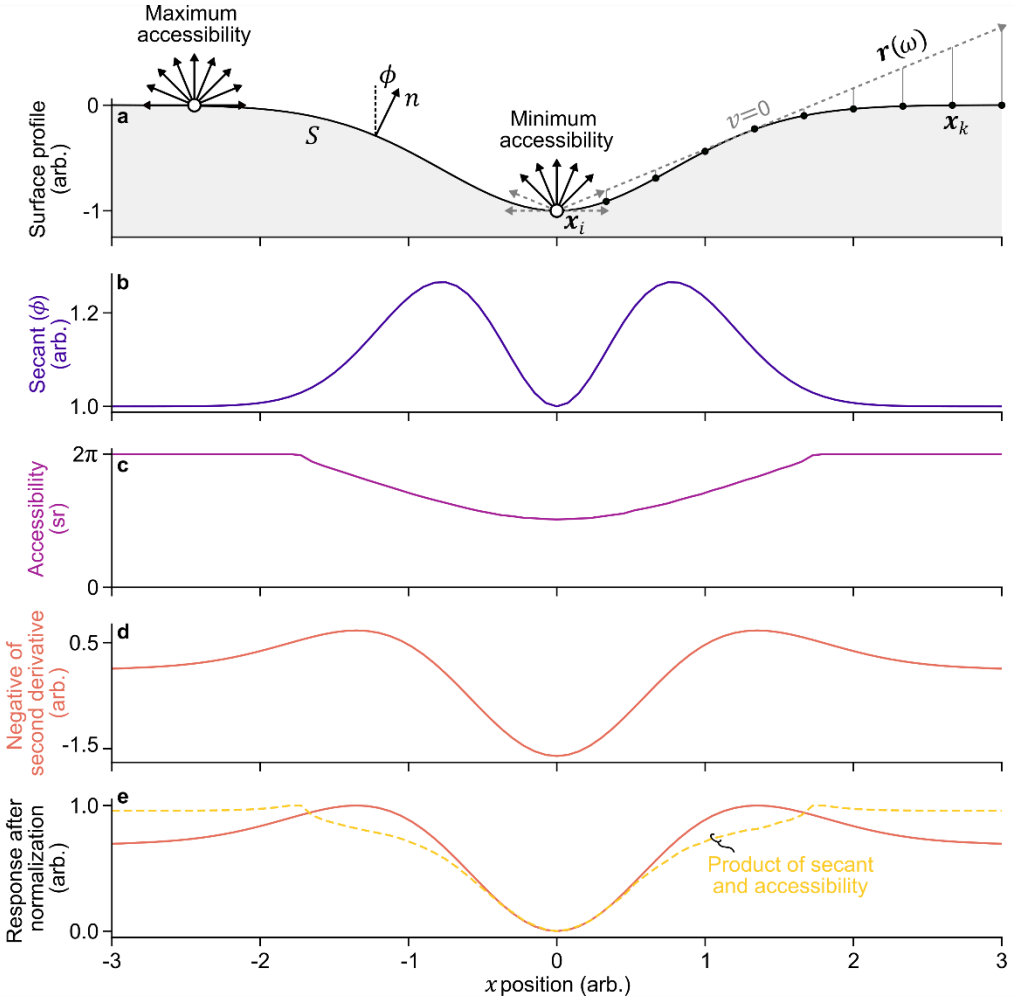

Figure S2. Image formation. Plots showing a) an arbitrary surface profile of a Gaussian pit, S, b) the secant of the tilt angle, ϕ, of the surface profile normal, n, c) accessibility of the surface profile, d) the negative of the second derivative of the surface profile, and e) an overlay of (solid orange line) the negative of the second derivative and (yellow dash line) the product of $\sec\phi$ and accessibility. Black arrows in (a) indicate rays that escape the surface and gray dash arrows indicate rays that the surface occludes. Abrupt changes in (c) are artifacts from discretization of the computational domain and numerical integration.

Note S4. In-line resolution metrology

To measure pit radii in both scanning electron micrographs and atomic force micrographs, we localize pit centers using empirical model approximations and then localize maxima in radial sections of regions of interest of each pit. We propagate uncertainty through our analysis by perturbing position and image data in Monte-Carlo simulations of our measurements.

Our analysis begins by thresholding each micrograph and computing centroids of simply connected regions to obtain the approximate positions of each pit. To localize the center of each pit in each imaging mode, we fit model approximations to image data. In images of pits in atomic force micrographs, we approximate the depths by an asymmetric bivariate function, $G(x, y)$,

$$G(x,y) = A_{\mathrm{G}} \cdot \exp\left\{-\left(\frac{1}{2(1-\rho^2)}\left[\frac{(x-x_0)^2}{\sigma_x^2} - 2\rho\frac{(x-x_0)(y-y_0)}{\sigma_x\sigma_y} + \frac{(y-y_0)^2}{\sigma_y^2}\right]\right)\right\} + c, \tag{S4}$$

where A_{G} is the amplitude, (x_0, y_0) is the center position of the pit in the x and y directions, σ_x and σ_y are the standard deviations in the x and y directions, ρ is the correlation coefficient between the x and y directions, and c is a constant background. In images of pits in scanning electron micrographs, we approximate the secondary-electron intensity as the sum of two functions. First, the Gaussian function in Equation (S4) approximates the intensity minimum at the center of a pit. Second, an elliptical annulus, $E(x, y)$, with the Gaussian profile in Equation (S5), approximates the ring of maximum intensity that circumscribes the center of the pit,

$$E(x,y) = A_{\mathrm{E}} \cdot \exp\left\{-\left(\frac{1}{2\omega^2(1-\rho^2)}\left[\frac{(x-x_0)^2}{\sigma_x^2} - 2\rho\frac{(x-x_0)(y-y_0)}{\sigma_x\sigma_y} + \frac{(y-y_0)^2}{\sigma_y^2} - 1\right]^2\right)\right\} + c, \tag{S5}$$

where A_{E} is the amplitude, ω is the width of the annulus. We estimate the localization uncertainties of the center of pit images by perturbing image and position data of either micrograph, fitting models to the resulting data, and extracting the resulting center positions. Repeating this process 10^3 times for each pit, we construct distributions of center positions from which we calculate standard deviations as localization uncertainties of center positions for each micrograph of each pit. We perturb values of position within regions of interest with random noise from uniform distributions, which correspond to lateral uncertainties from the probe tip for atomic force micrographs, or from magnification errors for scanning electron micrographs. We perturb values of the z position and intensity of secondary-electron scattering in regions of interest with random noise from normal distributions, which respectively correspond to errors in calibration, flatness, and various scanning artifacts for atomic force micrographs, or to estimates of the standard deviation of the background intensity of secondary-electron scattering for scanning electron micrographs, which we measure on the borders of regions of interest. This process of perturbing position and image data forms the basis of our Monte-Carlo simulation.

After localizing each pit, we align the array of pits in each micrograph by rotation of the micrographs so that the rows of pits in each micrograph are horizontal, corresponding to an angle of 0 rad. We then extract regions of interest of 1 by 1 μm and concentric with each pit from each micrograph. A symmetric bivariate Gaussian filter with an isotropic standard deviation ranging from 10 to 30 nm smooths image data within the region of interest (Table S3, Figure S3, Figure S4). To evaluate uncertainties of pit locations, we perturb the initial values of the center position of a pit with random noise from normal distributions of the localization uncertainty in the x and y directions. We excise one-dimensional sections of length 500 nm from the center position of the pit at an angle, θ, with respect to the horizontal direction of each image, for angles ranging from 0 to 2π rad. As before, we apply our Monte-Carlo simulation approach, perturbing the position and image data of these radial sections to propagate uncertainty through our analysis.

Both atomic force micrographs and scanning electron micrographs comprise discrete data with independent sources of noise that degrade images of the pits. Such noise complicates differentiation and may contribute to inaccurate measurements of the positions of extrema of the second derivative. To address this issue, we apply a Savitzky-Golay[12] digital smoothing filter with a cubic polynomial and a window length ranging from 13 to 27 pixels to smooth the one-dimensional sections and to enable second-order differentiation of the sections from atomic force micrographs (Table S3, Figure S3, Figure S4). We vary the window length of the filter to evaluate both random and systematic effects with respect to mean radius (Figure S4). Optimal window length depends primarily upon the signal-to-noise ratio present within an image and may vary with different imaging conditions.

After smoothing and differentiation, the sections from each micrograph include a single global maximum, with a position corresponding to the pit radius of the section. We model the local vicinity of the maximum with a quartic polynomial to localize the maximum of each radial section, $s(\theta)$. We define the angle-dependent radius of the pit in scanning electron micrographs, $r_{\mathrm{p,\,SEM}}(\theta)$, to be the distance between the center of the pit, $s_{0,\,\mathrm{SEM}}$, and the position of the maximum of the intensity of secondary electron scattering in scanning electron micrographs,

$$r_{\mathrm{p,\,SEM}}(\theta) = \underset{s(\theta)}{\arg\max}\left\{\boldsymbol{F}_{\mathrm{SG}}\left[\boldsymbol{F}_{\mathrm{G}}\left[\mathcal{N}\left(\mathcal{I}_{\mathrm{SE}}\left(s(\theta)\right), \sigma_{\mathrm{SE}}^2\right), \sigma_{\mathrm{G}}^2\right], \omega_{\mathrm{SG}}\right]\right\} - \mathcal{N}\left(s_{0,\,\mathrm{SEM}}, \sigma_{\mathrm{loc,\,SEM}}^2\right), \tag{S6}$$

where $\boldsymbol{F}_{\mathrm{SG}}$ denotes the application of the Savitzky-Golay filter with window length, ω_{SG}, $\boldsymbol{F}_{\mathrm{G}}$ denotes the application of the Gaussian filter with standard deviation σ_{G}, $\mathcal{N}$ denotes a normal distribution, $\mathcal{I}_{\mathrm{SE}}\left(s(\theta)\right)$ is the intensity of secondary electron scattering on the section, σ_{SE} is the standard deviation of the background intensity of secondary electron scattering,

$\sigma_{\text{loc, SEM}}$ is the localization uncertainty of the center of the pit, and the x and y components of the section on the sampling radius, r_s, $s(\theta) = (r_s\cos\theta, r_s\sin\theta)$, are each subject to uncertainty from a uniform distribution of $\mathcal{U}(-0.5\delta_{\text{mag}}, 0.5\delta_{\text{mag}})$ from the uncertainty of the magnification of the scanning electron micrographs, $\delta_{\text{mag}} = 0.03a_{\text{SEM}}$, where a_{SEM} is the mean value of pixel size of the scanning electron micrograph. Similarly, we define the angle-dependent radius of the pit in scanning electron micrographs, $r_{\text{p, AFM}}(\theta)$, to be the distance between the center of the pit, $s_{0,\text{ AFM}}$, and the position of the maximum value of convexity of the pit in atomic force micrographs,

$$r_{\text{p, AFM}}(\theta) = \underset{s(\theta)}{\arg\max}\left\{-\frac{\partial^2}{\partial s^2}\boldsymbol{F}_{\text{SG}}\left[\boldsymbol{F}_{\text{G}}\left[\mathcal{N}\left(z\left(s(\theta)\right), \sigma_{\text{cal}}^2\right) + \mathcal{N}(0, \sigma_{\text{r}}^2) + \mathcal{N}(0, \sigma_{\text{f}}^2), \sigma_{\text{G}}^2\right], \omega_{\text{SG}}\right]\right\} - \mathcal{N}\left(s_{0,\text{ AFM}}, \sigma_{\text{loc, AFM}}^2\right), \quad \text{(S7)}$$

where $z\left(s(\theta)\right)$ is the z position on the section, $\sigma_{\text{cal}} = 0.0025z$ accounts for a 0.5% systematic error from calibration of the atomic force microscope, σ_{r} accounts for uncertainty from the configuration of scan rate, scan resolution, and probe tip,[2] σ_{f} accounts for flatness errors, and the x and y components of the section, $s(\theta) = (r_s\cos\theta, r_s\sin\theta)$, are subject to uncertainty from a uniform distribution of $\mathcal{U}(-0.5r_{\text{tip}}, 0.5r_{\text{tip}})$ from the probe tip, where r_{tip} is the radius of the tip.

For each imaging mode, we repeat these measurements 30 times for angles ranging from 0 to 2π rad in increments of approximately 100 mrad. To propagate uncertainty, we perturb the position and image data with random noise from uncertainty parameters each time, resulting in 1860 measurements of radius for each pit, and a total of 18600 measurements for each set of 10 replicates. We record measurements of radius from all Monte-Carlo simulations, compiling distributions of radii for all replicates in each micrograph. Table S3 summarizes all statistical variables that are relevant to the Monte-Carlo simulation of the measurements of pit radii.

Our in-line measurements and topographic analyses of test pits are highly relevant for focusing and calibrating electron–ion beam systems. Moreover, our methods of image analysis are broadly applicable to localizing features and inferring dimensions of similar nanostructures in scanning electron micrographs.

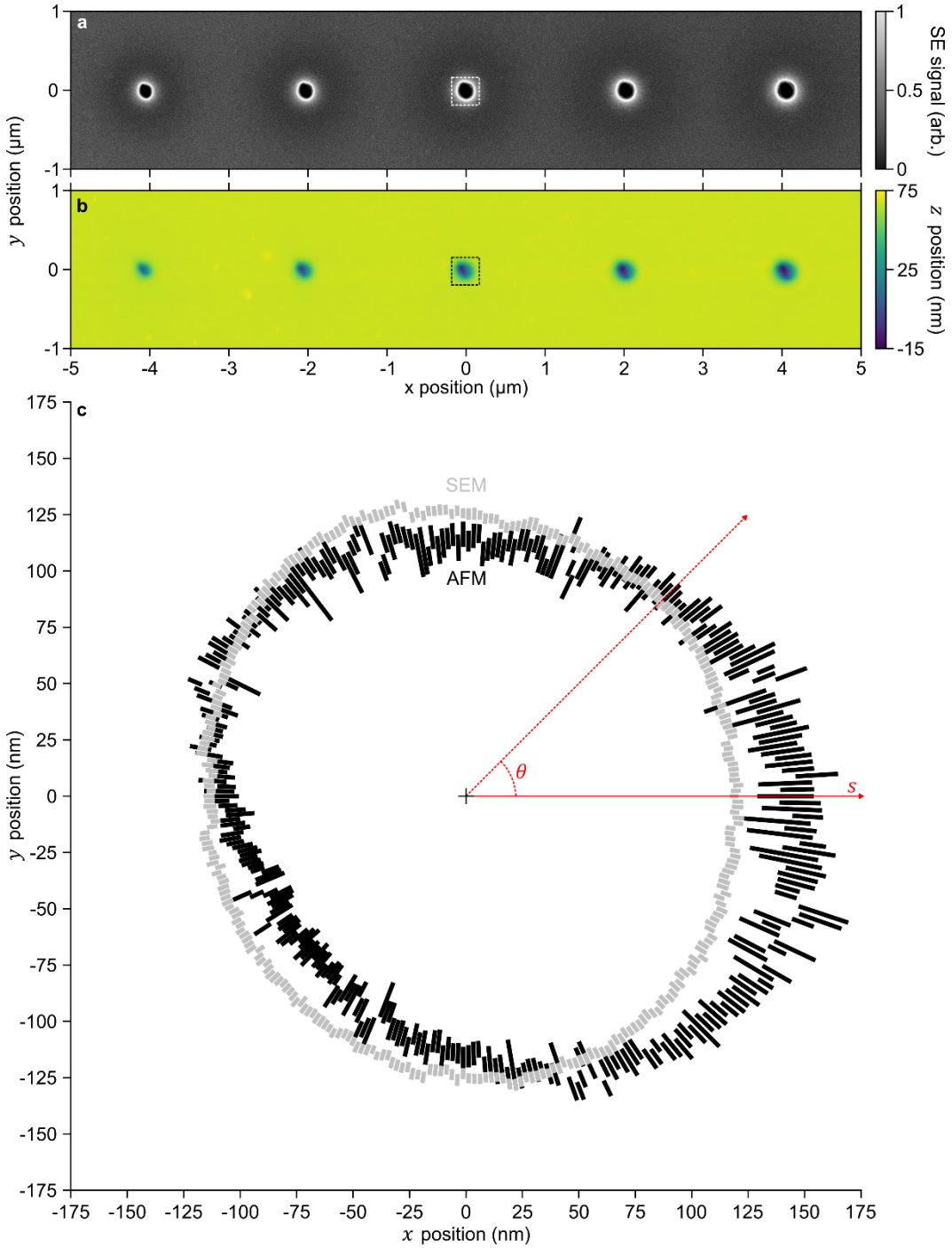

Figure S3. Correlative measurements. a) Scanning electron and b) atomic force micrographs showing the same representative array of pits that we mill with a focused ion beam with an ion-beam current of 219 ± 2 pA for dwell times ranging from 0.25 to 1.25 s in increments of 0.25 s. Dash boxes indicate the same region of interest in (c). c) Plots showing measurements of pit radius by (black) AFM and (gray) SEM for section angles ranging from 0 to 2π rad in increments of 20 mrad. The mean radius of the pit is 122 ± 4 nm by atomic force microscopy and 122 ± 1 nm by scanning electron microscopy. Bars indicate radius distribution widths as 95% coverage intervals.

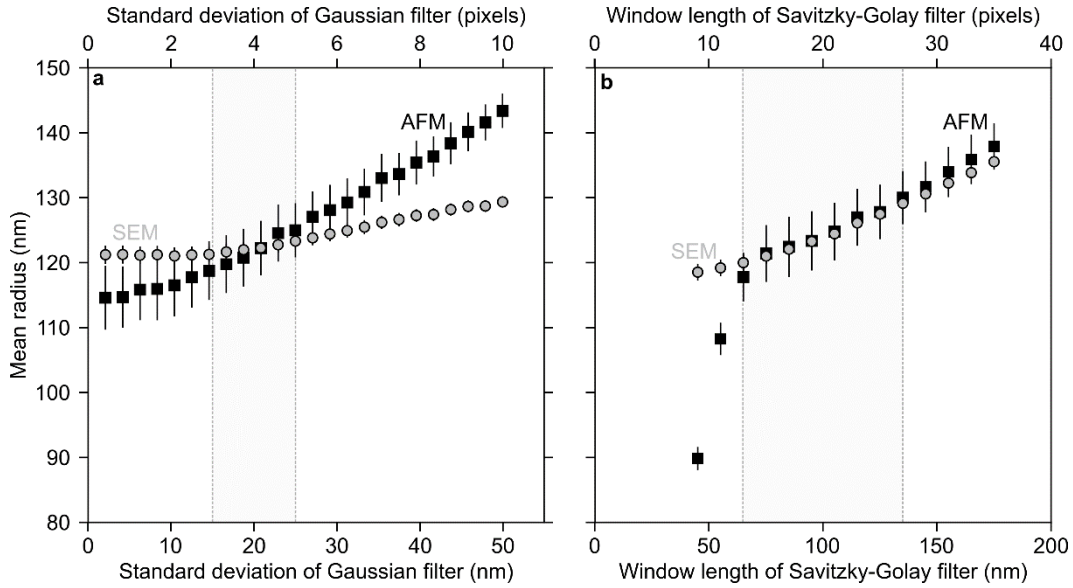

Figure S4. Filter parameters. a, b) Plots showing measurements of mean radius of a pit by (gray circles) scanning electron microscopy (SEM) and (black squares) atomic force microscopy (AFM) as functions of a) the standard deviation of the symmetric bivariate Gaussian filter and b) the window length of the Savitzky-Golay digital smoothing filter for the central pit in Figure S3a,b. Single values of the standard deviation of the Gaussian filter in (a) pair with a uniform distribution of the window length of the Savitzky-Golay filter in 1240 Monte-Carlo simulations of pit radius to isolate the effect of the value of standard deviation on measurements of pit radius. Similarly, single values of the window length of the Savitzky-Golay filter in (b) pair with a uniform distribution of the standard deviation of the Gaussian filter in 1240 Monte-Carlo simulations of pit radius to isolate the effect of the value of window length on measurements of pit radius. Gray dash lines indicate experimental ranges of the standard deviation of the Gaussian filter and the window length of the Savitzky-Golay filter (Table S3). These plots show the potential of each filter parameter to bias the measurements. Our simultaneous use of a range of values for each filter parameter yields measurements of mean pit radius in the center of these ranges with uncertainties of approximately 1 nm for scanning electron microscopy and 4 nm for atomic force microscopy.

Note S5. Milling Responses

We measure the depth, surface roughness, and edge width of the square features of checkerboard test-structures by analysis of atomic force micrographs. We level the atomic force micrographs and propagate uncertainties by Monte-Carlo simulations (Table S3). For each square feature, we extract image data from regions of interest of size 0.36 by 0.36 µm, or 30 by 30 pixels, and concentric with the center of the square. We perturb values of the z position with random noise from normal distributions to account for errors in calibration, flatness, and scanning artifacts for atomic force micrographs. We compute the mean depth and root-mean-square value of surface roughness of the flat of each square. For each edge in the scanning dimension of a square feature, we extract image data from five sections within regions of interest of size 1 by 0.36 µm, or 82 by 30 pixels. For each section, we propagate uncertainties from measurements by Monte-Carlo simulation and account for errors from systematic deviations in residuals from fits of models of step edges to data with leave-one-out jack-knife resampling.[13] We iteratively exclude one data point from the section and perturb all remaining values of position within this section with random noise from a uniform distribution corresponding to the lateral uncertainty from the radius of the probe tip. We perturb values of z position with random noise from normal distributions to account for errors from calibration, flatness, and scanning artifacts. We use an error function to empirically model the z position, $z_{\text{before}}(s)$, in sections of atomic force micrographs that transition from the bottom of a feature that we mill to the top of the chromia surface before chromia removal, Equation (S8),

$$z_{\text{before}}(s) = \frac{d}{2}\left[\text{erf}\left(\frac{s - s_0}{\sqrt{2}\sigma_{\text{edge}}}\right) + 1\right] + c, \tag{S8}$$

and we use an error function that we truncate at the zero plane to empirically model the same features after chromia removal, Equation (S9),

$$z_{\text{after}}(s) = \begin{cases} d \cdot \text{erf}\left(\frac{s - s_0}{\sqrt{2}\sigma_{\text{edge}}}\right) + c & s \le s_0, \\ c & s > s_0 \end{cases} \tag{S9}$$

where d is the depth of the feature, s_0 is the location of the edge, σ_{edge} is the standard deviation of a Gaussian, c is a constant, and s is subject to uncertainty from a uniform distribution of $\mathcal{U}(-0.5r_{\text{tip}}, 0.5r_{\text{tip}})$ from the radius of the probe tip. We approximate the width of edges as the 95% coverage interval of the width of the error functions, which correspond to $w_{\text{before}} = 4\sigma_{\text{edge}}$ before chromia removal and $w_{\text{after}} = 2\sigma_{\text{edge}}$ after chromia removal. We repeat this measurement 820 times for each section, retaining all fit parameters. This sampling results in a total of 8200 measurements of the widths of edges for each square feature in the checkerboard patterns.

Table S4. Uncertainties and errors

	Measurement uncertainty		Estimate of error	
Ion-beam current (pA)	Uncertainty of mean radius by atomic force microscopy (nm)	Uncertainty of mean radius by scanning electron microscopy (nm)	Root-mean-square residual to line of equality (nm)	Root-mean-square error (nm)
82 ± 1	3.1 ± 0.6	1.0 ± 0.1	3.7 ± 1.7	3.8 ± 1.8
219 ± 2	4.1 ± 1.9	1.0 ± 0.1	3.6 ± 1.6	6.7 ± 1.6
407 ± 2	6.5 ± 3.8	1.0 ± 0.1	3.4 ± 1.6	4.9 ± 1.1
773 ± 3	7.4 ± 4.4	1.0 ± 0.1	5.5 ± 2.6	5.8 ± 1.4

Uncertainties of ion-beam current are conservative estimates of 100% coverage intervals.

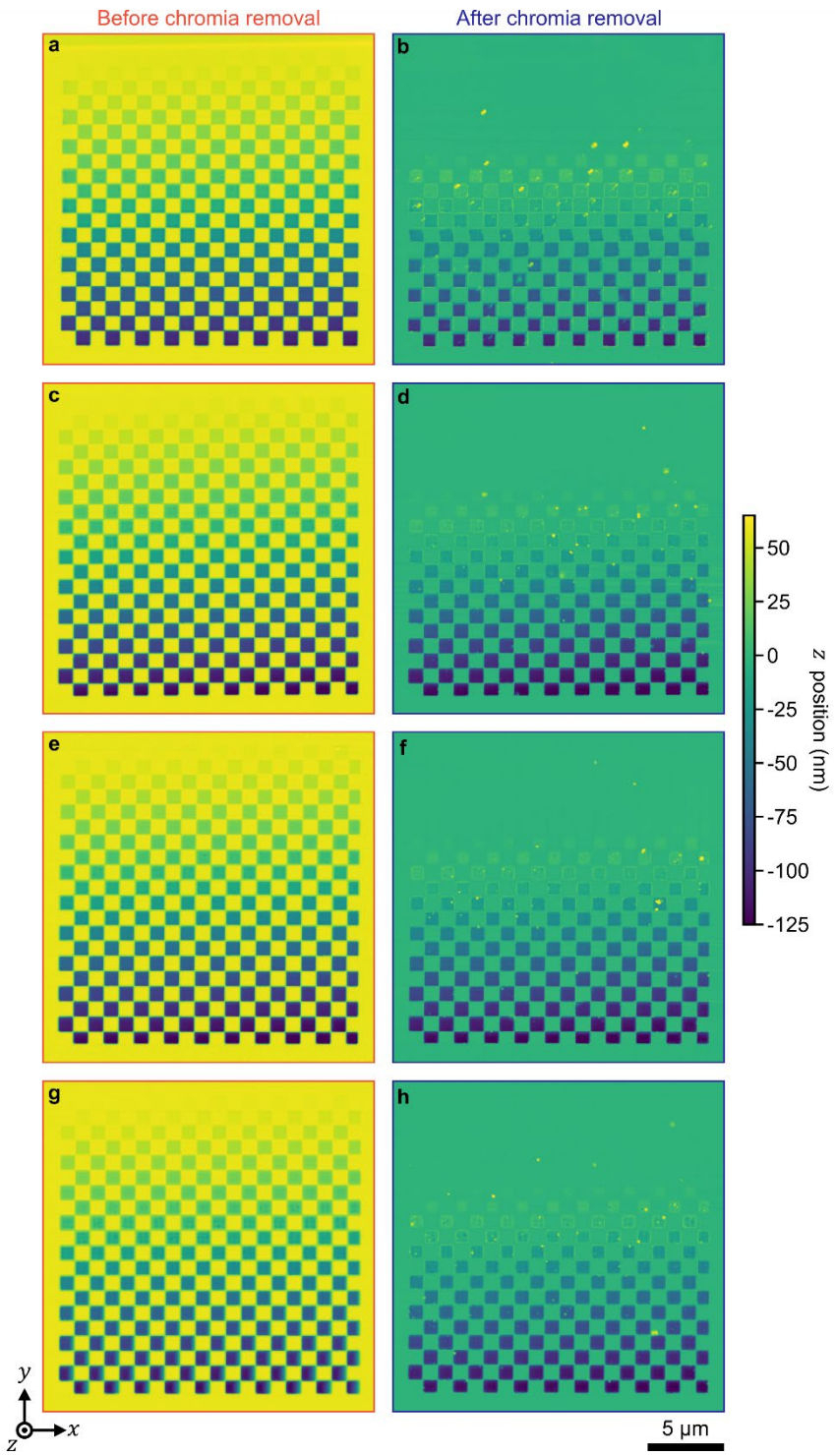

Figure S5. Complex test-structures. a-h) Atomic force micrographs showing checkerboard structures before and after chromia removal for several values of ion-beam current: (a,b) 83 ± 1 pA; (c,d) 227 ± 1 pA; (e,f) 421 ± 3 pA; and (g,h) 796 ± 4 pA. Uncertainties of ion-beam current are conservative estimates of 100% coverage intervals.

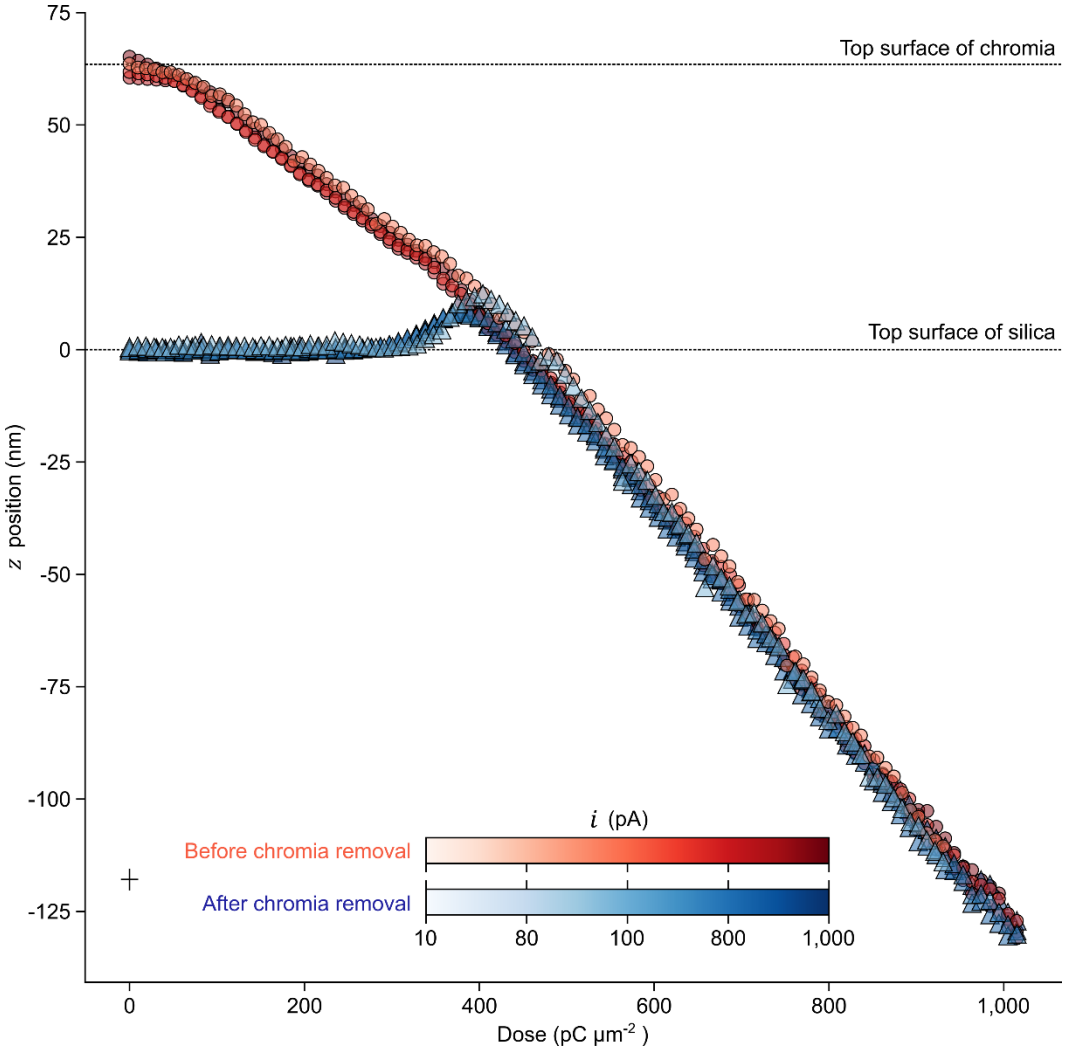

Figure S6. Vertical control. Plot showing milling responses of chromia and silica for a range of ion-beam currents (red circles) before and (blue triangles) after chromia removal. The color codes are logarithmic. The lone black cross near the lower left corner of the plot indicates a 100% coverage interval of dose and a 95% coverage interval of depth.

Table S5. Depth increments

Ion-beam current (pA)	Depth increment before removal of chromia mask		Depth increment after removal of chromia mask	
	Mean (nm)	Standard deviation (nm)	Mean (nm)	Standard deviation (nm)
83 ± 1	1.11 ± 0.22	1.23 ± 0.18	1.19 ± 0.24	0.94 ± 0.14
227 ± 1	1.13 ± 0.16	0.99 ± 0.10	1.18 ± 0.16	0.93 ± 0.10
421 ± 3	1.14 ± 0.12	0.91 ± 0.08	1.17 ± 0.14	0.99 ± 0.08
796 ± 4	1.14 ± 0.12	0.98 ± 0.06	1.16 ± 0.12	0.97 ± 0.06

Uncertainties of ion-beam current are conservative estimates of 100% coverage intervals.

Table S6. Milling responses

Segment	Material	Dose offset (pC µm^{-2})	*z* position (nm)	Milling rate (µm^3 nA^{-1} s^{-1})	Intercept (nm)
–	–	0 ± 0	63 ± 1	–	–
1	Top surface of silica	69 ± 6	59 ± 1	0.05 ± 0.03	66 ± 2
2	Bulk silica	366 ± 10	16 ± 3	0.15 ± 0.04	101 ± 10
3	Chromia–silica interface	531 ± 10	-16 ± 4	0.19 ± 0.04	126 ±11
4	Bulk chromia	1020 ± 0	-132 ± 6	0.24 ± 0.04	170 ± 14

Table S7. Gallium penetration

			z direction				*x* and *y* directions			
Figure	*z* position (nm)	Chromia thickness (nm)	Mean (nm)	Standard deviation (nm)	Skew	Kurtosis	Mean (nm)	Standard deviation (nm)	Skew	Kurtosis
Figure 5c-i	59	59	13.9	5.7	0.4	0.1	0.0	4.6	0.0	0.5
Figure 5c-ii	16	16	15.3	7.9	1.0	1.0	0.0	5.3	0.0	1.3
Figure 5c-iii	-16	0	27.6	9.1	0.4	0.1	0.0	7.0	0.0	0.4

All simulations are of 10^5 gallium ions with a landing energy of 4.81 fJ (30 keV) at normal incidence, a chromia, Cr_2O_3, density of 5.3 g cm^{-3}, and a silica, SiO_2, density of 2.2 g cm^{-3}.

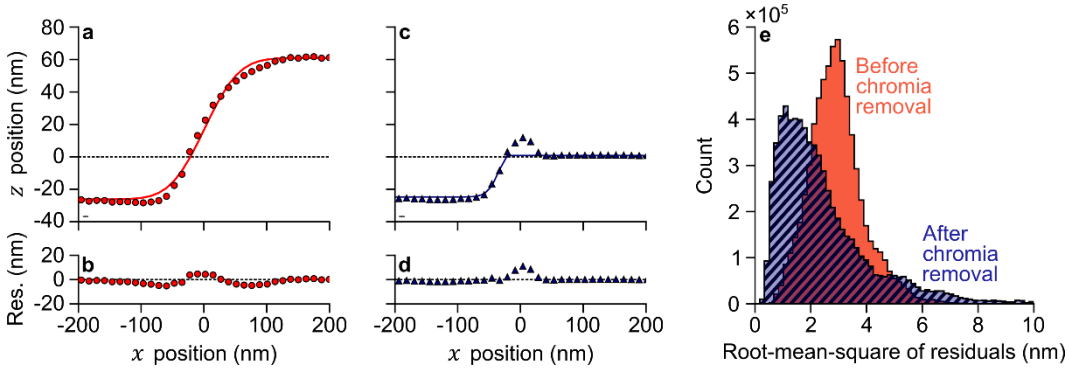

Figure S7. Model summary. a-d) Plots showing representative (a,c) model fits and (b,d) residuals (a,b) before, and (c,d) after chromia removal. Overshoot artifact is apparent in (c). The root-mean-square of residuals in (a,b) and (c,d) are respectively 1.9 and 2.0 nm. e) Histograms showing the root-mean-square of residuals of fits of all test structures and ion-beam currents. Lone black bars in (a) and (c) indicate representative uncertainties of *x* position as 95% coverage intervals. Uncertainties of *z* position are smaller than the data markers.

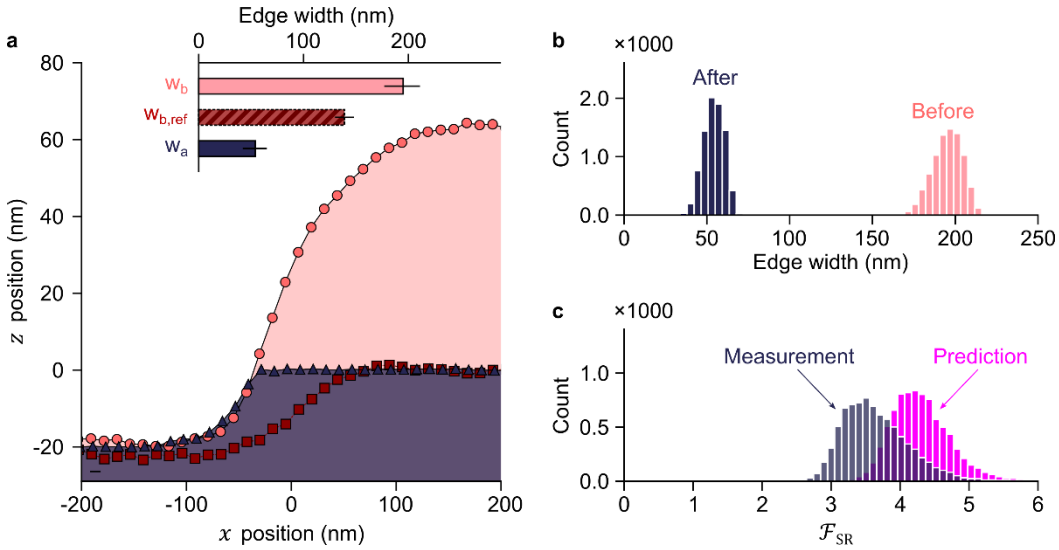

Figure S8. Measurement and prediction. a) Plots showing representative edge profiles. The solid regions show profiles resulting from a dose of 536 pC µm^{-2} and from an ion-beam current of 227 ± 1 pA, (red circles) before and (blue triangles) after removal of the chromia mask. The dark red squares are from a feature with a similar depth resulting from a dose of 189 pC µm^{-2} and from an ion-beam current of 227 ± 1 pA. The lone black bar in (a) indicates a representative uncertainty of *x* position as a 95% coverage interval. Uncertainties of *z* position are smaller than the data markers. The inset bar chart shows the edge width of each profile with black bars indicating edge width distributions as 95% coverage intervals. b) Histograms showing edge widths (light red) before and (dark blue) after removal of the chromia mask. c) Histograms showing super-resolution factors, $\mathcal{F}_{SR}$, from (dark blue) measurement and (magenta) prediction by the spatial masking model. Additional details are in Table S8.

Table S8. Measurement and prediction

Method	Depth (nm)	Depth after normalization by mask thickness	Edge width (nm)			Super-resolution factor ($\mathcal{F}_{SR}$)
			Before removal (w_b)	Before removal at reference depth ($w_{b,ref}$)	After removal (w_a)	
Measurement	$17.7\ ^{+0.8}/_{-0.9}$	$0.278\ ^{+0.014}/_{-0.014}$	$195\ ^{+16}/_{-18}$	$139\ ^{+9}/_{-9}$	$54\ ^{+11}/_{-12}$	$3.6\ ^{+1.2}/_{-0.7}$
Prediction	–	$0.278\ ^{+0.010}/_{-0.010}$	–	–	–	$4.3\ ^{+1.0}/_{-0.7}$

Fractional notation denotes 95% coverage intervals that are asymmetric.
The sample size is 830 for all values.

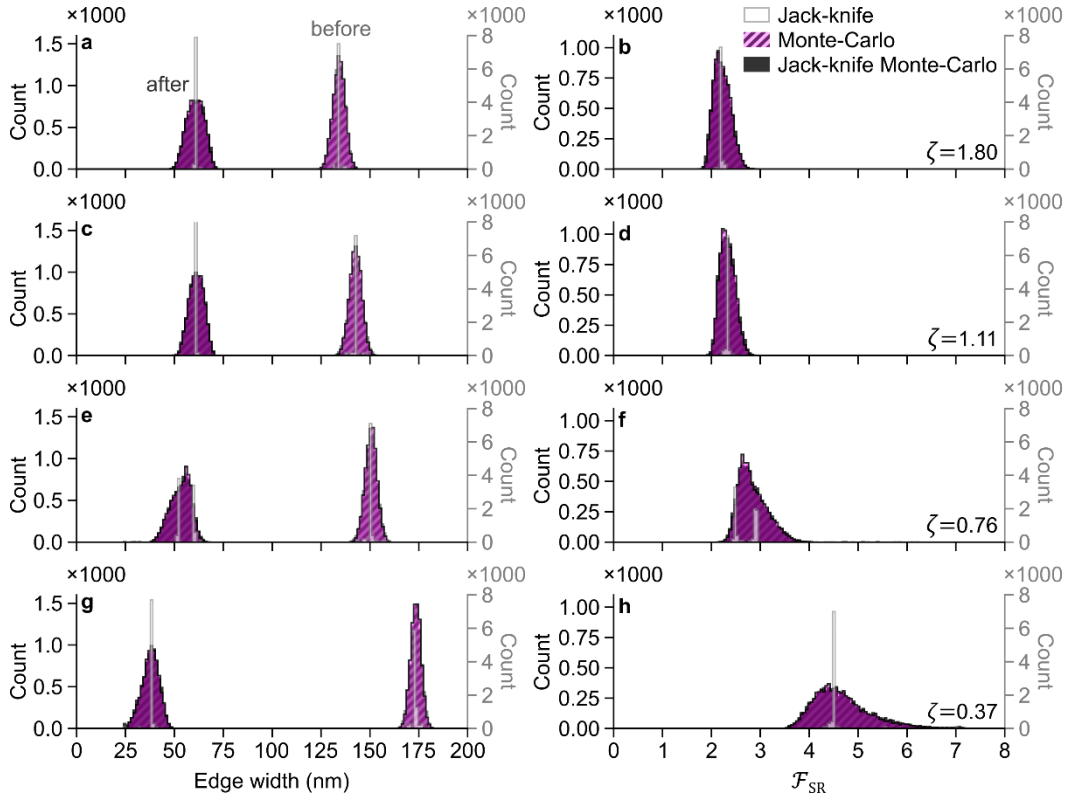

Figure S9. Numerical analysis. a,c,e,g) Histograms showing edge widths (light shading) before and (dark shading) after chromia removal and b,d,f,h) histograms showing super-resolution factors for three simulation and resampling methods: (white region with gray outline) jack-knife resampling only; (magenta and black hash region) Monte-Carlo simulation only; and (black region) jack-knife resampling with Monte-Carlo simulation. (a,b) A feature resulting from a dose of 561 ± 2 pC μm^{-2} and having a depth of 24 ± 1 nm. (c,d) A feature resulting from a dose of 663 ± 3 pC μm^{-2} and having a depth of 49 ± 1 nm. (e,f) A feature resulting from a dose of 765 ± 3 pC μm^{-2} and having a depth of 71 ± 2 nm. (g,h) A feature resulting from a dose of 969 ± 4 pC μm^{-2} and having a depth of 114 ± 4 nm. In each panel, counts of distributions from the Monte-Carlo and jack-knife Monte-Carlo methods correspond to vertical axes on the left, and counts of distributions from the jack-knife method correspond to vertical axes on the right. Depths after normalization by mask thickness appear in the lower right corner of panels (b,d,f,h). Additional details are in Table S9.

Table S9. Numerical analysis

Method	Feature number	Samples	Depth		Super-resolution factor	
			Mean (nm)	Mean after normalization (–)	Mean (–)	Standard deviation (–)
Jack-knife	110	8300	23.7 ± 0.02	0.373 ± 0.0004	4.531 ± 0.006	0.302 ± 0.003
Monte-Carlo	110	8300	23.6 ± 0.02	0.372 ± 0.0004	4.660 ± 0.012	0.564 ± 0.008
Jack-knife Monte-Carlo	110	8300	23.7 ± 0.02	0.373 ± 0.0004	4.691 ± 0.014	0.618 ± 0.010
Jack-knife	130	8300	48.2 ± 0.03	0.759 ± 0.0004	2.709 ± 0.004	0.206 ± 0.004
Monte-Carlo	130	8300	48.2 ± 0.03	0.760 ± 0.0004	2.857 ± 0.006	0.290 ± 0.004
Jack-knife Monte-Carlo	130	8300	48.2 ± 0.03	0.760 ± 0.0004	2.862 ± 0.008	0.316 ± 0.005
Jack-knife	150	8300	70.8 ± 0.03	1.115 ± 0.0006	2.325 ± 0.001	0.026 ± 0.001
Monte-Carlo	150	8300	70.8 ± 0.04	1.115 ± 0.0006	2.336 ± 0.004	0.151 ± 0.002
Jack-knife Monte-Carlo	150	8300	70.8 ± 0.03	1.115 ± 0.0006	2.339 ± 0.004	0.157 ± 0.002
Jack-knife	190	8300	114.3 ± 0.05	1.801 ± 0.0008	2.212 ± 0.001	0.021 ± 0.001
Monte-Carlo	190	8300	114.3 ± 0.05	1.800 ± 0.0008	2.222 ± 0.004	0.167 ± 0.002
Jack-knife Monte-Carlo	190	8300	114.3 ± 0.05	1.800 ± 0.0008	2.220 ± 0.004	0.172 ± 0.002

Table S10. Edge widths

Metric	Ion-beam current (pA)							
	83 ± 1		227 ± 1		421 ± 3		796 ± 4	
	Before (nm)	After (nm)	Before (nm)	After (nm)	Before (nm)	After (nm)	Before (nm)	After (nm)
2.5th percentile	117	32	116	51	127	64	137	66
25th percentile	133	43	135	67	157	83	165	94
Mean	142	54	154	79	174	101	195	113
75th percentile	148	59	171	84	185	105	221	132
97.5th percentile	173	87	216	117	241	165	276	179

Uncertainties of ion-beam current are conservative estimates of 100% coverage intervals.
Uncertainties of values of percentiles[14] are all less than 1 nm.

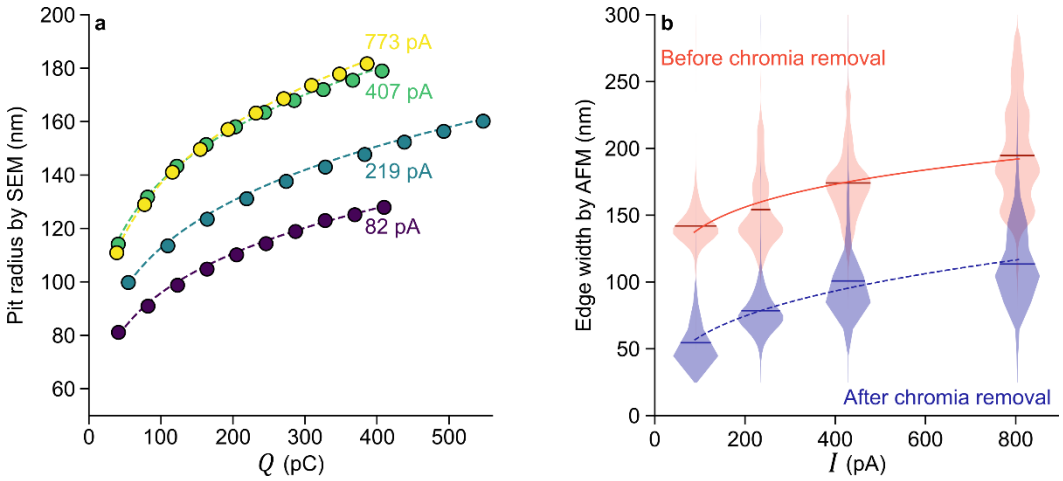

Figure S10. Patterning resolution. a) Plot showing pit radius by scanning electron microscopy as a function of charge, Q, with fits of power-law models. The non-monotonic trend in pit radius as a function of ion-beam current shows imperfections in the reproduction of ion-beam focus due to manual operation of the system, motivating development of methods for complete automation of ion-beam focusing, which our study of in-line resolution metrology enables. b) Plot showing edge width by atomic force microscopy before chromia removal as a function of ion-beam current, I. Violin plots show distributions of edge widths from complex test-structures below the zero plane, corresponding to the metrics in Table S10 for edge widths (red) before and (blue) after removal of chromia. The dark lines in violin plots indicate mean values. The solid and dash lines indicate representative fits of power-law models to data.

Table S11. Symbols, values, and definitions

Symbol	Range of values	Units	Definition
I	83 to 796	pA	Ion-beam current
z	−150 to 65	nm	z position of edge profile resulting from exposure of substrate to a focused ion beam
z_m	61 to 65	nm	Mask thickness
z_s	0 to 150	nm	Milling depth into the substrate
ζ	0 to 2.2	–	Milling depth into the substrate after normalization by mask thickness, $\zeta = \lvert z \rvert z_\mathrm{m}^{-1}$
$\bar{m}_\mathrm{m}$	0.11 to 0.19	–	Average milling rate of the mask
$\bar{m}_\mathrm{s}$	0.20 to 0.28	–	Average milling rate of the substrate
$\mathcal{S}$	1.0 to 2.1	–	Physical selectivity, the ratio of average milling rates of the substrate, $\mathcal{S} = \bar{m}_\mathrm{s}\bar{m}_\mathrm{m}^{-1}$
w_b	116 to 276	nm	Width of nanostructure edges before removal of the mask
w_a	32 to 179	nm	Width of nanostructure edges after removal of the mask
$\mathcal{F}_\mathrm{SR}$	1 to 6	–	Super-resolution factor, ratio of widths of step edges before and after removal of the mask, $\mathcal{F}_\mathrm{SR} = w_\mathrm{b}w_\mathrm{a}^{-1}$
$\mathcal{R}$	32 to 276	nm	Effective lateral patterning resolution or super-resolution
V_m	0.000 to 0.065	μm^3	Volume of the mask that the ion-beam mills for each square feature of the complex test-structures
V_s	0.000 to 0.150	μm^3	Volume of the substrate that the ion-beam mills for each square feature of the complex test-structures
$\mathcal{V}$	55 to 530	μm^3 hr^{-1}	Volume throughput of material that the ion-beam mills per unit time
α	34 to 86	nm pA$^{-\beta}$	Coefficient in power-law model of the widths of step edges with respect to ion-beam current
β	0.1 to 0.3	–	Exponent in power-law model of the widths of step edges with respect to ion-beam current
η_τ	10^{-1} to 10^5	–	Temporal efficiency, ratio of milling times in the absence, t_s, and presence, $t_\mathrm{s} + t_\mathrm{m}$, of a mask, $\eta_\tau = t_\mathrm{s}(t_\mathrm{s} + t_\mathrm{m})^{-1}$
$\mathcal{M}$	10^2 to 10^5	μm^2 hr^{-1}	Figure of merit for focused-ion-beam milling, $\mathcal{M} = \mathcal{V}\,\mathcal{R}^{-1}$

Note S6. Bi-Gaussian approximation

Under the conditions that are necessary to mill a semi-infinite edge, an error function is a good approximation of the total dose pattern from both Gaussian and bi-Gaussian approximations of the current density distribution of a focused ion beam. The bi-Gaussian[15] model, $BG(x; A, \sigma_\mathrm{core}, \sigma_\mathrm{tail}, \omega, x_i)$, in Equation (S10) accounts for contributions to the total current density from both the core and the tails of the ion beam in a summation of two Gaussian functions,

$$BG(x; A, \sigma_\mathrm{core}, \sigma_\mathrm{tail}, \omega, x_i) = A\left[\omega \exp\left\{-\frac{(x - x_i)^2}{2{\sigma_\mathrm{core}}^2}\right\} + (1 - \omega)\exp\left\{-\frac{(x - x_i)^2}{2{\sigma_\mathrm{tail}}^2}\right\}\right], \tag{S10}$$

where A is the amplitude of the ion beam dose, ω is a parameter that varies between 0 and 1 to weight the Gaussian components, σ_core is the standard deviation of the core of the ion beam, σ_tail is the standard deviation of the tail of the ion beam, and x_i is the milling location of the ion beam. Equation (S10) reduces to a Gaussian model when $\omega = 1$. Models of the ion-beam shape and size inform discrete positioning of the ion beam during the direct-write process of focused-ion-beam milling. In particular, the full-width at half-maximum of the core of the ion beam is a common approximation of the diameter of the ion beam, $d_\mathrm{beam} = 2\sqrt{2\ln(2)}\sigma_\mathrm{core}$. The diameter of the ion beam and the overlap, o, define the pitch or spacing of adjacent milling positions in a rectilinear coordinate system, $\Delta x = (1 - o)d_\mathrm{beam}$. As such, a semi-infinite dose pattern comprises a series of milling positions that occur with equal spacing, Δx, on the half-line in one-dimensional space. As previous studies[8, 16] show, an overlap greater than or equal to 0.35 ensures the delivery of a uniform dose in the bulk of the half-line.

Our study of spatial masking motivates an inquiry into the effect of the bi-Gaussian approximation of the profile of a focused ion beam on the edge of a semi-infinite dose pattern. In particular, the deviation from an error function of a semi-infinite dose pattern that the bi-Gaussian model imposes is of interest. We model a semi-infinite dose pattern in one dimension, $D(x)$, as a series of discrete milling locations of a focused ion beam that follows the bi-Gaussian approximation,

$$D(x) = \frac{D_0}{D_N}\sum_i^N BG(x; A, \sigma_\mathrm{core}, \sigma_\mathrm{tail}, \omega, x_i), \tag{S11}$$

where D_0 is the value of dose in the bulk of the half-line and D_N is a factor that normalizes the maximum value of the summation in Equation (S11) to unity. To quantify the deviation of the semi-infinite dose pattern from an error function, we simulate dose patterns for ratios of σ_tail to σ_core ranging from 1 to 10, a range of weights ranging from 0 to 0.5, an amplitude of the bi-Gaussian model of 1, and an overlap of 0.5 (50%). We fit an error function,

$$D(x) = \frac{D_0}{D_N}\sum_i^N BG(x; A, \sigma_\mathrm{core}, \sigma_\mathrm{tail}, \omega, x_i) \cong D_0\left[1 - \frac{1}{2}\left(\mathrm{erf}\left(\frac{x - x_0}{\sqrt{2}\sigma_\mathrm{eff}}\right) + 1\right)\right], \tag{S12}$$

the resulting dose patterns, where σ_eff is the effective standard deviation of the edge of the dose pattern and x_0 is the position of the center of the edge. For each parameterization, we compute the root-mean-square error between each dose pattern and its corresponding fit.

Values of root-mean-square error are less than 2.5% for all parameterizations of the focused-ion-beam shape (Figure S11). This good agreement indicates a general consistency between the bi-Gaussian approximation of the current density distribution of a focused ion beam and the error function model of the semi-infinite dose pattern that results from milling in discrete positions, which supports the validity of our use of the error function in our model of the lateral super-resolution effect.

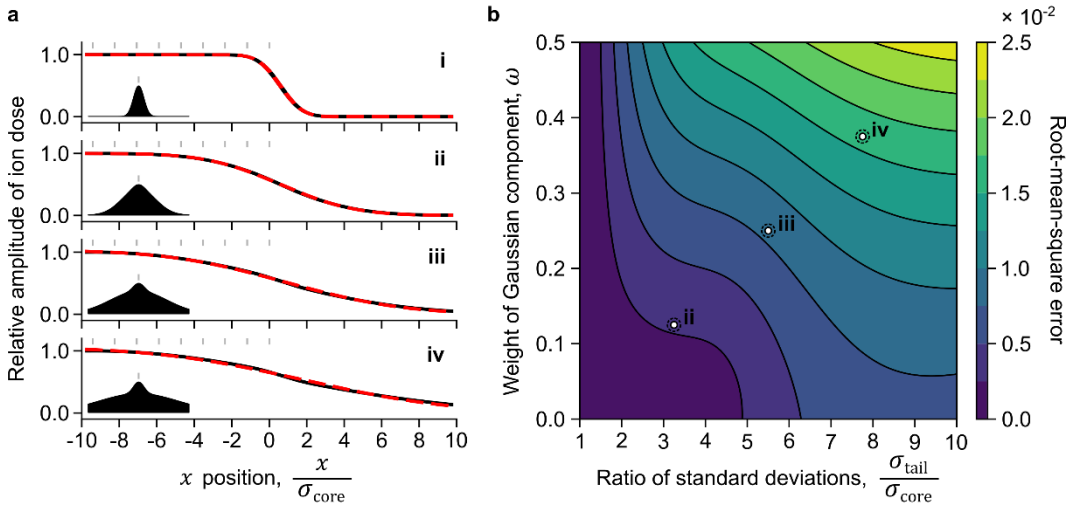

Figure S11. Bi-Gaussian approximation. a) Plots showing (solid black line) the relative amplitude of ion dose resulting from milling an array of (gray ticks) discrete positions and (red dash line) fits of the error function in Equation (S12) for four combinations of values of $\sigma_{\text{tail}}\sigma_{\text{core}}^{-1}$ and ω: (i) $\sigma_{\text{tail}}\sigma_{\text{core}}^{-1} = 1.00$, $\omega = 1.000$; (ii) $\sigma_{\text{tail}}\sigma_{\text{core}}^{-1} = 3.25$, $\omega = 0.125$; (iii) $\sigma_{\text{tail}}\sigma_{\text{core}}^{-1} = 5.5$, $\omega = 0.250$; and (iv) $\sigma_{\text{tail}}\sigma_{\text{core}}^{-1} = 7.75$, $\omega = 0.375$. The insets of panels (a-i–a-iv) show the spatial profile of the ion beam over the extents of the spatial domain, $\pm 10\sigma_{\text{core}}$, for each parameterization. b) Contour plot showing root-mean-square error of fits of the error function to relative dose profiles for a subset of the parameter space of the bi-Gaussian function. The position on the contour plot of the Gaussian profile in (a-i) is beyond the vertical extent of the plot. The root-mean-square error of fits of the error function to the relative dose profile corresponding to the Gaussian profile is zero.

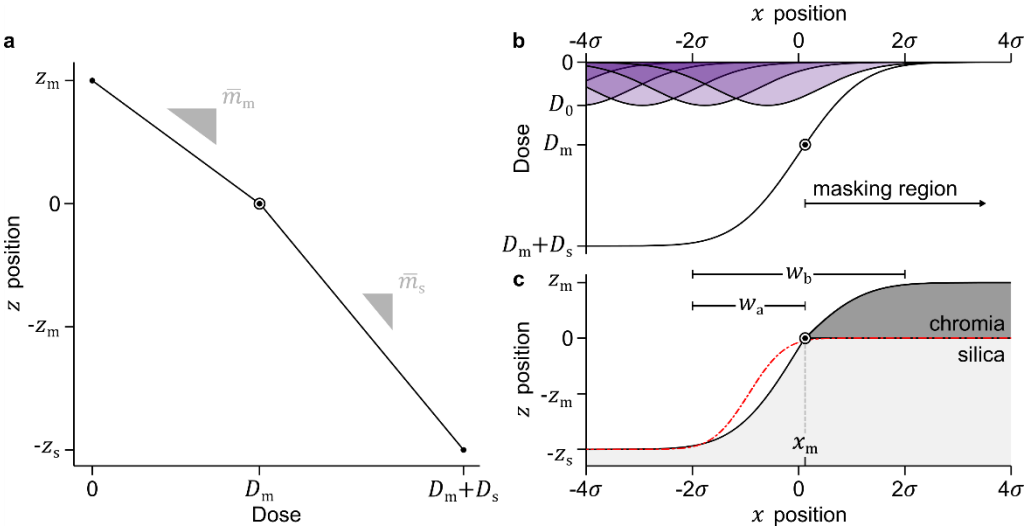

Figure S12. Spatial masking. a) Plot showing z position as a function of dose for a simple model of milling in which a sacrificial mask of thickness, z_m, and average milling rate, $\bar{m}_m$, screens a substrate with an average milling rate of $\bar{m}_s$. b) Plot showing spatial ion-dose pattern from (violet) discrete positions of an ion beam as a function of x position. c) Plot showing (solid black line) a theoretical surface profile resulting from application of the dose in (b) to the milling model in (a). The red dash-dot line is a theoretical surface profile that results from the application of a dose of similar magnitude to that in (b) but from a lower value of ion current and milling directly into the silica substrate. Consequently, the red profile has a different shape from the black profile. After removal of the chromia mask, both profiles have an edge width of $2\sigma + x_m$. The red profile includes the entire transition region of the sigmoid of the dose profile, whereas after removal, the black profile shows truncation of a sigmoid. The black and the red profiles are simplifications that neglect the dependence of incidence angle on milling rate, any effects of redeposition, and any defocus of the ion-beam due to charging. However, the standard deviation of the ion-beam that yields the black profile, which has the greater value of current, is $\sigma_{high} = \sigma$ while the standard deviation of the ion-beam that yields the red profile is $\sigma_{low} = 0.53\sigma$. An exponent of $\beta = 0.2$ in the power-law model from Equation (1) implies a ratio of the two currents of $\left(\sigma_{high}\sigma_{low}^{-1}\right)^{1/\beta}$, or approximately 24.

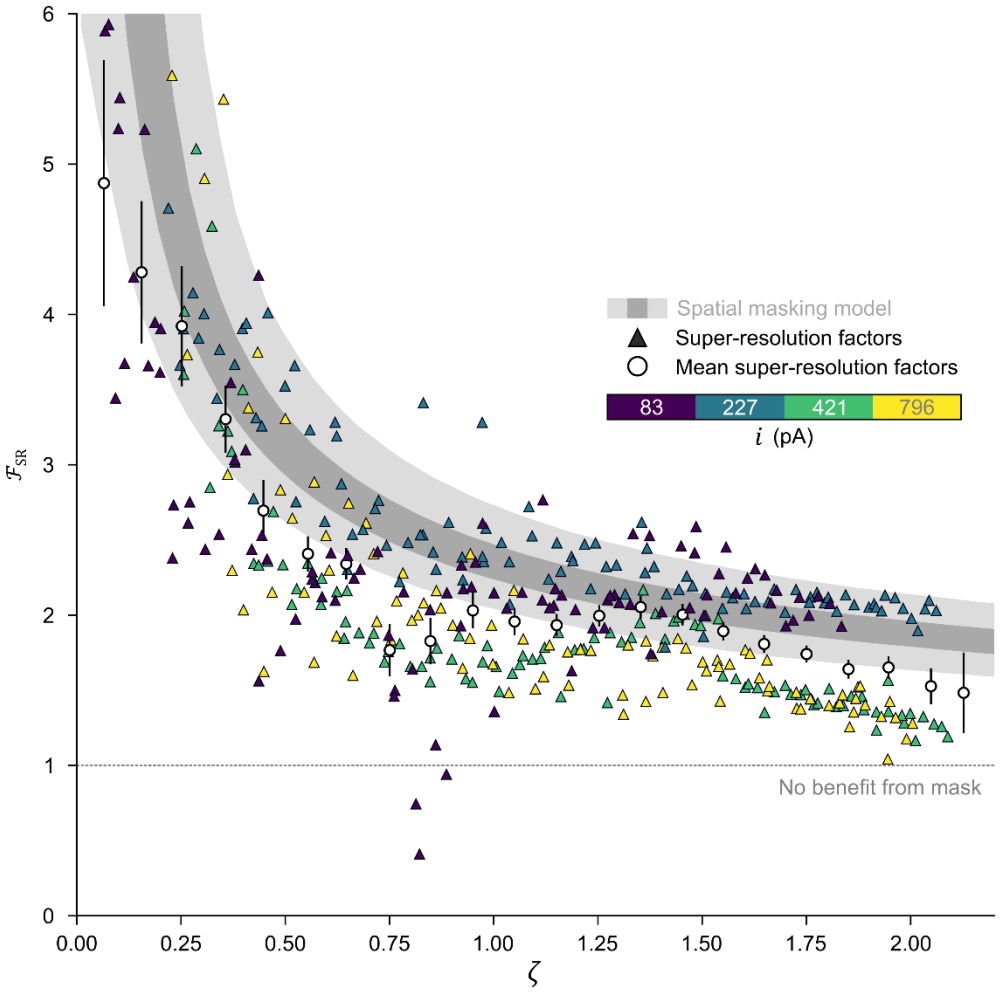

Figure S13. Super-resolution. Plot showing values of super-resolution factors, $\mathcal{F}_{SR}$, as a function of the ratio of milling depth into the substrate after normalization by mask thickness, ζ, for features below the zero plane resulting from four values of ion-beam current. The light and dark gray shading respectively indicate the 95% coverage interval and the interval between the lower and upper quartiles of the spatial masking model. The triangles are features that we mill with ion-beam currents that range from approximately 80 to 800 pA. The white circles are mean super-resolution factors from the entire data set. For clarity, we show only a fraction of these values. The black bars indicate uncertainties of mean super-resolution factor as 95% coverage intervals. Uncertainties of ζ are smaller than the data markers.

Note S7. Spatial masking of a line or point

We derive an analytic expression for the spatial limit of a sacrificial mask to screen the tails of ion beam from an underlying substrate during exposure in one dimension. We apply the resulting model to fit the experimental data of Menard and Ramsey,[17] with several simplifying assumptions. We assume that the mask has a bulk milling rate, m_m, and a thickness, z_m, and similarly, that the substrate has a bulk milling rate, m_s, and a final depth, z_s, and that the spatial profile of the ion dose along the x direction, $D(x)$, follows a Gaussian function of the form,

$$D(x) = D_0 \exp\left\{-\frac{(x - x_0)^2}{2\sigma^2}\right\}, \tag{S13}$$

where D_0 is the dose that is necessary to mill through the mask and into the working material, x_0 is the center position of the line scan, which we assign to be 0, and σ is the effective standard deviation of the Gaussian profile of the ion beam. Substitution into Equation (S13) of $D_0 = D_m + D_s = z_m m_m^{-1} + z_s m_s^{-1}$, the ratio of milling depth of the substrate to the thickness of the mask, $\zeta = z_s z_m^{-1}$, and the ratio of the milling rate of the substrate to the milling rate of the mask, $\mathcal{S} = m_s m_m^{-1}$, yields the condition for spatial masking of the dose pattern, where

$$D_m = \frac{z_m}{m_m} = \left[\frac{z_m}{m_m} + \frac{z_s}{m_s}\right] \exp\left\{-\frac{x^2}{2\sigma^2}\right\} = \frac{z_m m_s + z_s m_m}{m_m m_s} \exp\left\{-\frac{x^2}{2\sigma^2}\right\}, \tag{S14}$$

which implies

$$\frac{\mathcal{S}}{\mathcal{S}+\zeta} = \exp\left\{-\frac{x^2}{2\sigma^2}\right\}. \tag{S15}$$

Solving Equation (S15) for x yields the positions at which the mask begins to screen the tails of the ion beam,

$$x = \pm\sigma\sqrt{-2\ln\left(\frac{\mathcal{S}}{\mathcal{S}+\zeta}\right)}. \tag{S16}$$

The diameter of a pit or the width of a nanochannel resulting after removal of the sacrificial mask is the distance between these positions,

$$w_\mathrm{a} = 2\sigma\sqrt{-2\ln\left(\frac{\mathcal{S}}{\mathcal{S}+\zeta}\right)}. \tag{S17}$$

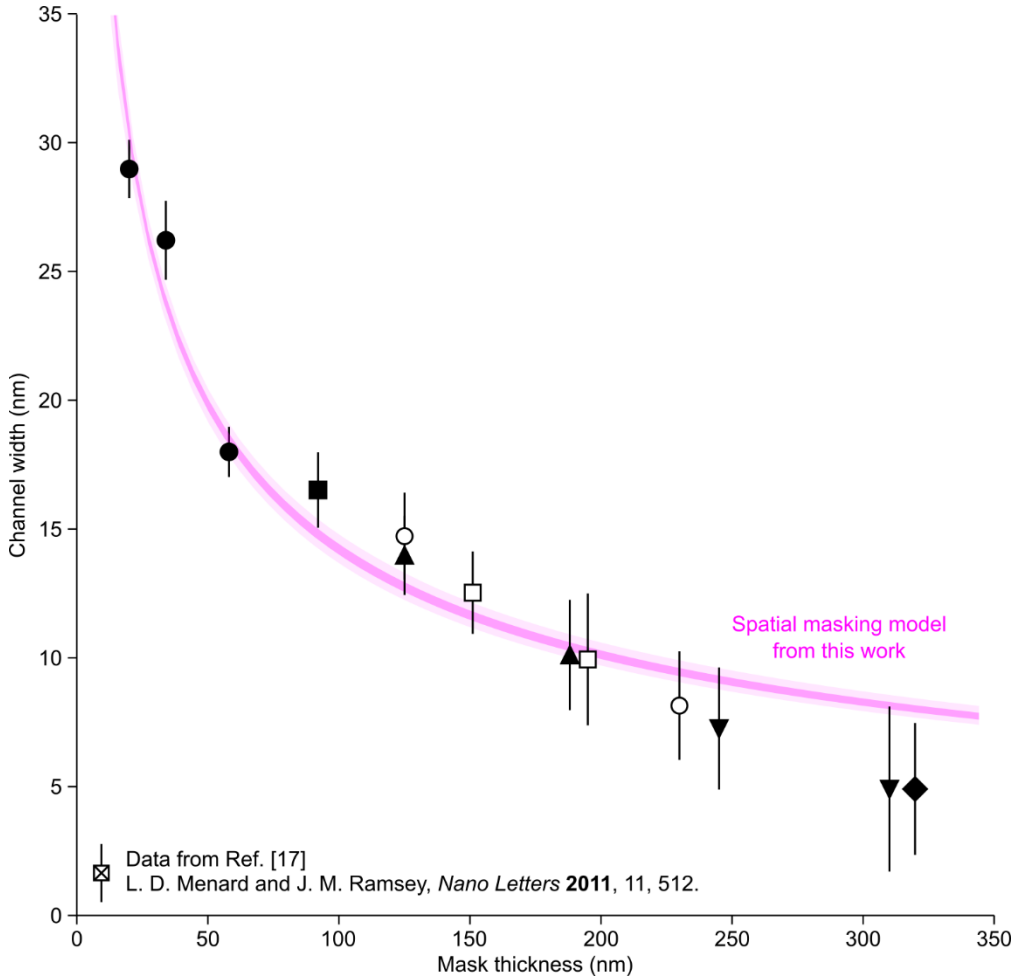

Figure S14. Comparison to a previous study. Plot showing widths of channels as a function of the thickness of sacrificial masks of chromium after removal of the mask. The channels result from the spatial masking of line scans of a focused beam of gallium ions, milling through sacrificial chromium masks and into underlying quartz substrates. The data markers show the experimental results from Menard and Ramsey.[17] Using approximate values of experimental parameters from correspondence with these scholars, we bound the values of the effective standard deviation of the ion beam to the range from 20 to 60 nm, the milling depth parameter to the range from 0 to 20 nm, and the value of the physical selectivity parameter to the range from 0 to 3, and we fit our spatial masking model of a line scan in Equation (S17). This fit yields a reduced chi-square statistic, χ_ν^2, of 5.3, extracts reasonable values of experimental parameters including standard deviation of the ion-beam profile, milling depth, and physical selectivity, and indicates that our spatial masking model is generally applicable beyond the specific system in our current study. The light and dark magenta regions indicate uncertainties of mean channel width respectively as 95% coverage intervals and interquartile ranges of fit results to our spatial masking model. This analysis yields estimates of experimental parameters, including an effective standard deviation of the ion beam of 46 $^{+14\ \mathrm{nm}}/_{-15\ \mathrm{nm}}$, a milling depth of 7.8 $^{+3.9\ \mathrm{nm}}/_{-4.2\ \mathrm{nm}}$, and a physical selectivity of quartz to chromium of 1.5 $^{+1.0}/_{-0.6}$. Uncertainties of these parameters and of the data markers are 95% coverage intervals.

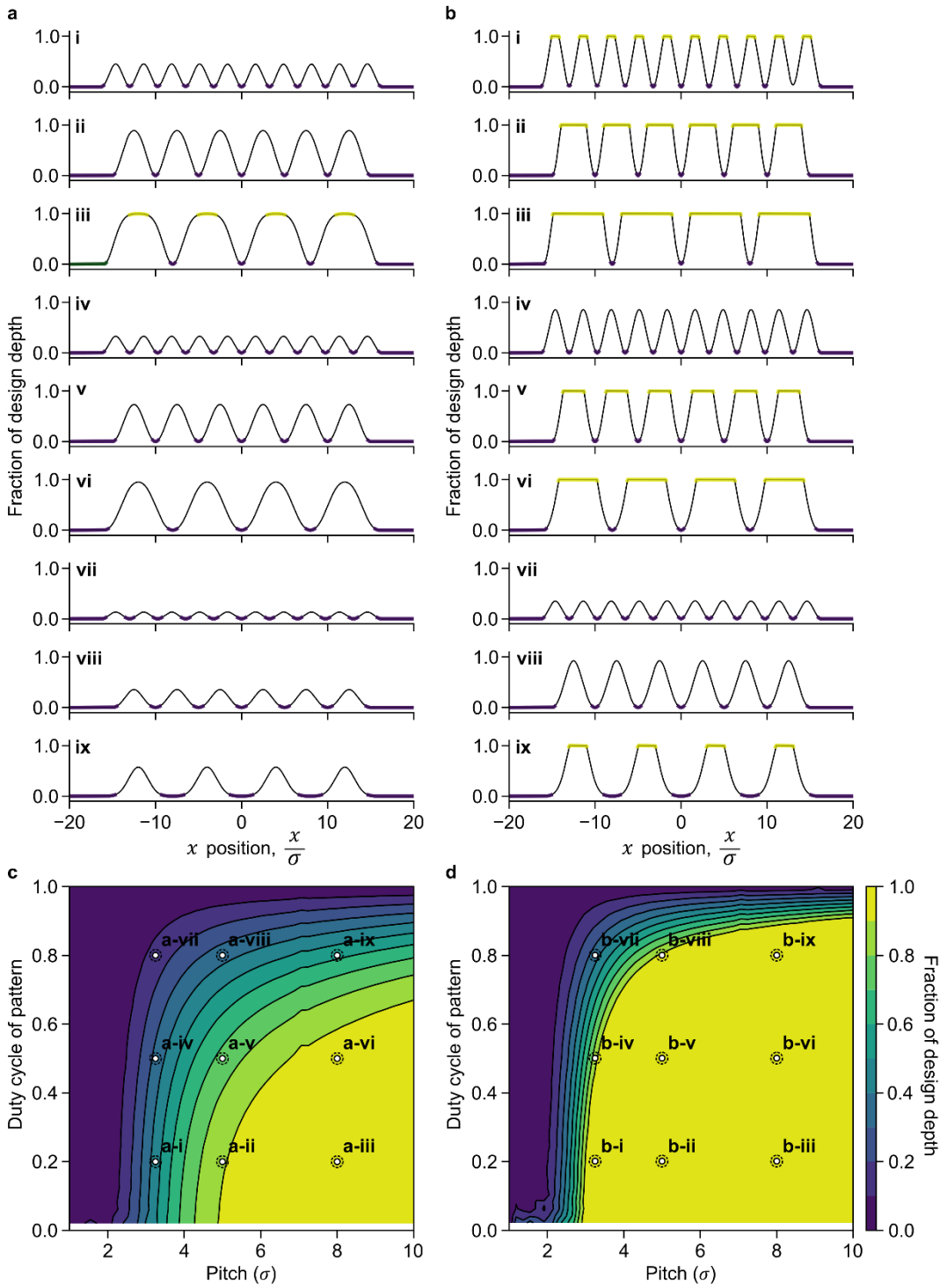

Figure S15. Line–space patterns. Plots showing theoretical profiles of lines and spaces that result from a) direct milling of silica and b) milling of silica through a sacrificial mask of chromia for nine combinations of pitch, ranging from 3.25σ to 8σ, and duty cycle, ranging from 20% to 80%. Purple regions indicate the floor of the profile. Yellow regions indicate segments of profiles that exceed a tolerance threshold of 0.975. The profiles in (a) are ideal cases which neglect the dependence of incidence angle on milling rate, any effects of redeposition, and any defocus of the ion-beam due to charging. c) Contour plot showing the fraction of design depths for the set of profiles in panels (a-i–a-ix) that result from the direct milling of silica. d) Contour plot showing the fraction of design depth for the set of profiles in panels (b-i–b-ix) that result from milling of silica through a sacrificial mask of chromia. Our selection of nine combinations of pitch and duty cycle highlights the transition regions in both contour plots. In each contour plot, a sampling artifact, which is inconsequential to our analysis, is aparent for values of pitch of approximately 7σ.

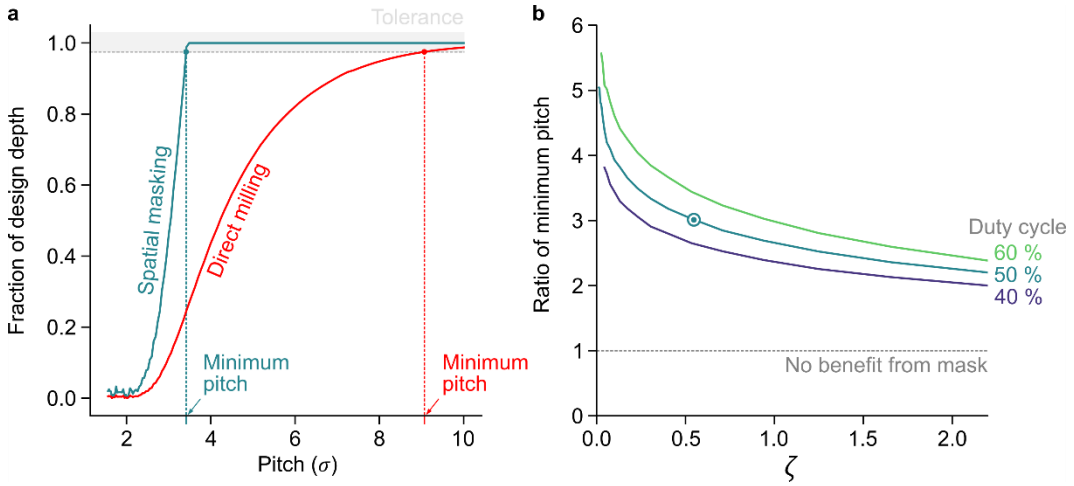

Figure S16. Minimum pitch ratio. a) Plot showing fraction of design depth as a function of pitch at a duty cycle of 50% and a design depth of $\zeta \approx 0.5$ for (solid green line) milling of silica with a sacrificial mask of chromia and (solid red line) direct milling of silica. The trends in (a) represent ideal cases that neglect the dependence of incidence angle on milling rate, any effects of redeposition, and any defocus of the ion-beam due to charging. The gray dash line indicates a tolerance threshold of 0.975. The green and red vertical dash lines respectively indicate a minimum pitch for spatial masking of approximately 3σ and a minimum pitch for direct milling of approximately 3σ, yielding a ratio of minimum pitch of 3. b) Plot showing ratios of minimum pitch as a function of milling depth for duty cycles ranging from 40% to 60%. The green roundel corresponds to the simulation result in (a).

Note S8. Temporal efficiency

The time that is necessary to mill a certain nanostructure is typically inversly proportional to ion-beam current. Consequently, simply reducing the ion-beam current to improve lateral patterning resolution can dramatically increase the milling time. Furthermore, multicurrent processes involving a high current to mill coarse structures and a low current to mill fine structures increase the complexity of the process, requiring realignment after switching between the two ion beams, and can still require long milling times, depending on constraints of lateral resolution. These issues motivate our study of the temporal efficiency of sacrificial masking of a focused ion beam.

We derive an analytic expression for temporal efficiency, defining the theoretical condition for which the use of a sacrificial mask and a high value of ion-beam current is faster than milling a structure with similar edge width directly into the substrate by use of a lower value of ion-beam current. We assume that the nominal radius of the ion-beam follows a power law approximation, $r_{\text{beam}} \cong \alpha I^{\beta}$, where α is a constant, I is the ion-beam current, and the scaling exponent, β, typically ranges from 0.3 to 1 for ion-beam currents of less than 10 nA.[18] In the absence of a sacrificial mask, the lateral resolution is, $\mathcal{R} \cong r_{\text{beam}}$. The presence of a sacrificial mask improves the lateral resolution by a multiplicative super-resolution factor, $\mathcal{F}_{\text{SR}}$, where $\zeta = |z_{\text{s}}|z_{\text{m}}^{-1}$ is the ratio of the depth of the nanostructure, z_{s} to the thickness of the mask, z_{m}, and $\mathcal{S} = \bar{m}_{\text{s}}\bar{m}_{\text{m}}^{-1}$ is the physical selectivity of the substrate and the mask, which we define as the ratio of their average milling rates, $\bar{m}_{\text{s}}$ and $\bar{m}_{\text{s}}$, respectively. We consider an equality of lateral resolution from a low value of ion-beam current, I_{low}, and lateral super-resolution from a high value of ion-beam current, I_{high}, milling through a sacrificial mask. Then,

$$\mathcal{R} = \alpha i_{\text{low}}^{\beta} = \mathcal{F}_{\text{SR}}^{-1}\alpha I_{\text{high}}^{\beta}, \tag{S18}$$

which implies generally that

$$\mathcal{F}_{\text{SR}}\left(\sigma_{\text{low}}, \sigma_{\text{high}}, \tilde{z}, \mathcal{S}\right) = \left(\frac{I_{\text{high}}}{I_{\text{low}}}\right)^{\beta}. \tag{S19}$$

The condition of equivalent edge widths for the high and low values of ion-beam current from Equations (11) and (12) imply that

$$w_{\text{low}} = w_{\text{high}} = 4\sigma_{\text{low}} = \sqrt{2}\sigma_{\text{high}}\text{erf}^{-1}\left(1 - \frac{2\mathcal{S}}{\mathcal{S}+\zeta}\right) + 2\sigma_{\text{high}} = \sigma_{\text{high}}\left[\sqrt{2}\,\text{erfc}^{-1}\left(\frac{2\mathcal{S}}{\mathcal{S}+\zeta}\right) + 2\right], \tag{S20}$$

where we apply the identity, $\text{erf}^{-1}(1-x) = \text{erfc}^{-1}(x)$. The power-law approximation of the radius of the ion beam relates our model of super-resolution factor from Equation (13) to values of ion-beam current that are necessary to achieve equivalent lateral resolution,

$$\left(\frac{I_{\mathrm{high}}}{I_{\mathrm{low}}}\right)=\left(\frac{\sigma_{\mathrm{high}}}{\sigma_{\mathrm{low}}}\right)^{\frac{1}{\beta}}=\left(\frac{2}{\frac{1}{\sqrt{2}}\mathrm{erfc}^{-1}\left(\frac{2\mathcal{S}}{\mathcal{S}+\zeta}\right)+1}\right)^{\frac{1}{\beta}}=\mathcal{F}_{\mathrm{SR}}(\zeta,\mathcal{S})^{\frac{1}{\beta}}. \tag{S21}$$

The time that is necessary to mill a nanostructure of arbitrary rectangular volume, V_{s}, through the sacrificial mask, t_{M}, with a high value of ion-beam current is the sum of the time that is necessary to mill through the chromia mask, t_{m}, and the time that is necessary to mill the underlying substrate, t_{s},

$$t_{\mathrm{M}}=t_{\mathrm{m}}+t_{\mathrm{s}}\approx\frac{V_{\mathrm{m}}}{\overline{m}_{\mathrm{m}}I_{\mathrm{high}}}+\frac{V_{\mathrm{s}}}{\overline{m}_{\mathrm{s}}I_{\mathrm{high}}}=\frac{z_{\mathrm{m}}l^2}{\overline{m}_{\mathrm{m}}I_{\mathrm{high}}}+\frac{z_{\mathrm{s}}l^2}{\overline{m}_{\mathrm{s}}I_{\mathrm{high}}}, \tag{S22}$$

where l^2 is the area of the rectangular nanostructure and V_{m} is the volume of the mask above the milling area. For clarity, $\overline{m}_{\mathrm{m}}$ and have $\overline{m}_{\mathrm{s}}$ units of volume per current per second or $\mu m^3\ nA^{-1}\ s^{-1}$. Therefore, in Equation (S22), dividing a volume by the product of a milling rate and ion-beam current yields a value with units of time. In contrast, the time that is necessary to mill a similar nanostructure directly into the substrate with a low value of ion-beam current is

$$t_{\mathrm{s}}\approx\frac{V_{\mathrm{s}}}{\overline{m}_{\mathrm{s}}I_{\mathrm{low}}}=\frac{z_{\mathrm{s}}l^2}{\overline{m}_{\mathrm{s}}I_{\mathrm{low}}}. \tag{S23}$$

We define the temporal efficiency, η_τ, to be the ratio of these milling times,

$$\eta_\tau=\frac{t_{\mathrm{s}}}{t_{\mathrm{M}}}=\frac{\frac{z_{\mathrm{s}}l^2}{\overline{m}_{\mathrm{s}}I_{\mathrm{low}}}}{\frac{z_{\mathrm{m}}l^2}{\overline{m}_{\mathrm{m}}I_{\mathrm{high}}}+\frac{z_{\mathrm{s}}l^2}{\overline{m}_{\mathrm{s}}I_{\mathrm{high}}}}=\left(\frac{I_{\mathrm{high}}}{I_{\mathrm{low}}}\right)\frac{z_{\mathrm{s}}\overline{m}_{\mathrm{m}}}{z_{\mathrm{m}}\overline{m}_{\mathrm{s}}+z_{\mathrm{s}}\overline{m}_{\mathrm{m}}}. \tag{S24}$$

Substitution of $z_{\mathrm{s}}=\zeta z_{\mathrm{m}}$, $\overline{m}_{\mathrm{s}}=\mathcal{S}\overline{m}_{\mathrm{m}}$, and Equation (S21) into Equation (S24) yields an analytic expression for the temporal efficiency, which we argue must be greater than unity for masking to be beneficial,

$$\eta_\tau=\left(\frac{I_{\mathrm{high}}}{I_{\mathrm{low}}}\right)\frac{\zeta}{\mathcal{S}+\zeta}=\mathcal{F}_{\mathrm{SR}}(\zeta,\mathcal{S})^{\frac{1}{\beta}}\frac{\zeta}{\mathcal{S}+\zeta}. \tag{S25}$$

Table S12. Power-law models

Tradespace	Model parameters α (nm ($\mu m^3\ h^{-1}$)$^{-\beta}$)	β (–)
Resolution	76.4 ± 0.1	0.154 ± 0.001
Super-resolution	16.2 ± 0.1	0.314 ± 0.010

Note S9. Milling currents of equivalent resolution
For two power law models, the condition of equivalent resolution is

$$\mathcal{R}_{\mathrm{R}}=\alpha_{\mathrm{R}}\mathcal{V}_{\mathrm{R}}^{\beta_{\mathrm{R}}}=\mathcal{R}_{\mathrm{SR}}=\alpha_{\mathrm{SR}}\mathcal{V}_{\mathrm{SR}}^{\beta_{\mathrm{SR}}}. \tag{S26}$$

Solving for $\mathcal{V}_{\mathrm{SR}}$ and accounting for the two different milling rates and thickness of the bilayer gives the volume throughput in terms of a high value of ion-beam current with equaivalent resolution,

$$\mathcal{V}_{\mathrm{SR}}=\left(\frac{\mathcal{R}_{\mathrm{SR}}}{\alpha_{\mathrm{SR}}}\right)^{\frac{1}{\beta_{\mathrm{SR}}}}=I_{\mathrm{high}}\left(\frac{z_{\mathrm{m}}+z_{\mathrm{s}}}{\frac{z_{\mathrm{m}}}{\overline{m}_{\mathrm{m}}}+\frac{z_{\mathrm{s}}}{\overline{m}_{\mathrm{s}}}}\right). \tag{S27}$$

Applying the right side of the power-law equation (S26) gives

$$\mathcal{V}_{\mathrm{SR}}=\left(\frac{\alpha_{\mathrm{R}}}{\alpha_{\mathrm{SR}}}\mathcal{V}_{\mathrm{R}}^{\beta_{\mathrm{R}}}\right)^{\frac{1}{\beta_{\mathrm{SR}}}}=I_{\mathrm{high}}\left(\frac{z_{\mathrm{m}}+z_{\mathrm{s}}}{\frac{z_{\mathrm{m}}}{\overline{m}_{\mathrm{m}}}+\frac{z_{\mathrm{s}}}{\overline{m}_{\mathrm{s}}}}\right). \tag{S28}$$

Applying the left side of equation (S26) and solving for I_{high},

$$I_{\mathrm{high}} = \left(\frac{\alpha_{\mathrm{R}}}{\alpha_{\mathrm{SR}}}\left[m_{\mathrm{s}} I_{\mathrm{low}}\right]^{\beta_{\mathrm{R}}}\right)^{\frac{1}{\beta_{\mathrm{SR}}}} \left(\frac{\frac{z_{\mathrm{m}}}{\bar{m}_{\mathrm{m}}} + \frac{z_{\mathrm{s}}}{\bar{m}_{\mathrm{s}}}}{z_{\mathrm{m}} + z_{\mathrm{s}}}\right). \tag{S29}$$

Conversely,

$$I_{\mathrm{low}} = \frac{1}{\bar{m}_{\mathrm{s}}}\left[\frac{\alpha_{\mathrm{SR}}}{\alpha_{\mathrm{R}}}\left(I_{\mathrm{high}} \frac{z_{\mathrm{m}} + z_{\mathrm{s}}}{\frac{z_{\mathrm{m}}}{\bar{m}_{\mathrm{m}}} + \frac{z_{\mathrm{s}}}{\bar{m}_{\mathrm{s}}}}\right)^{\beta_{\mathrm{SR}}}\right]^{\frac{1}{\beta_{\mathrm{R}}}}. \tag{S30}$$

Table S13. Factors of improvement

Ion-beam current (pA)	Before chromia removal			After chromia removal			Factor of improvement		
	Throughput (μm³ hr⁻¹)	Resolution (nm)	Figure of merit (μm² hr⁻¹)	Equivalent throughput (μm³ hr⁻¹)	Super-resolution (nm)	Figure of merit (μm² hr⁻¹)	Throughput	Resolution	Figure of merit
83 ± 1	54.5 ± 0.2	144.4 ± 0.2	385 ± 2	0.10 ± 0.02	53.9 ± 0.4	1112 ± 2	528 ± 28	2.678 ± 0.016	2.890 ± 0.006
227 ± 1	151.0 ± 0.2	160.7 ± 0.2	986 ± 2	1.25 ± 0.04	79.2 ± 0.2	2058 ± 4	119 ± 4	2.029 ± 0.006	2.088 ± 0.004
421 ± 3	280.7 ± 0.2	180.1 ± 0.2	1621 ± 2	5.52 ± 0.22	99.3 ± 0.6	3115 ± 6	51 ± 3	1.814 ± 0.010	1.921 ± 0.004
796 ± 4	529.8 ± 0.4	202.5 ± 0.2	2773 ± 4	12.72 ± 0.22	112.9 ± 0.2	5103 ± 10	42 ± 2	1.794 ± 0.004	1.840 ± 0.006

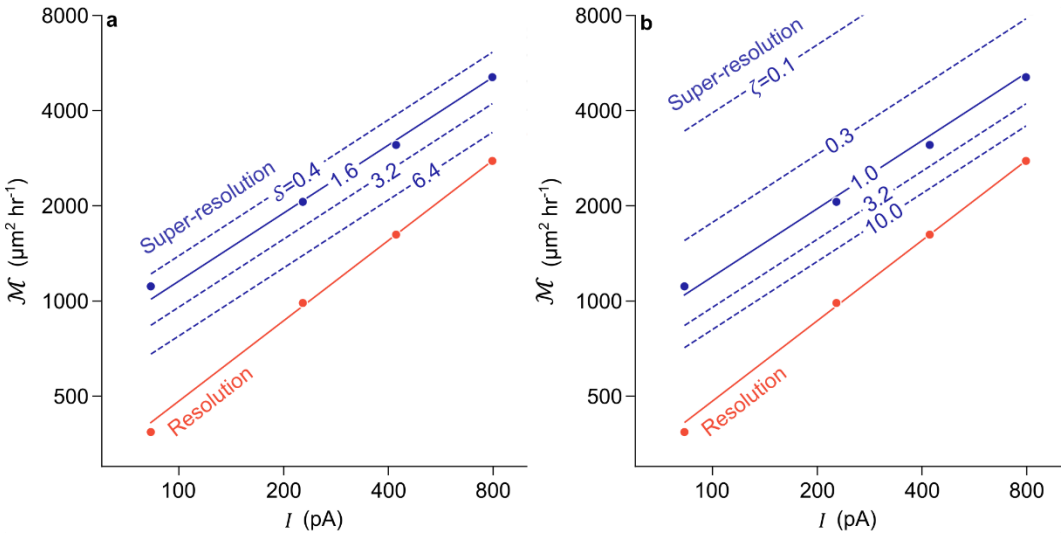

Figure S17. Figure of merit. a) Plot showing figure of merit, $\mathcal{M}$, as a function of ion-beam current, I, for a constant value of milling depth after normalization by mask thickness of $\zeta = 1$ and values of physical selectivity, $\mathcal{S}$, ranging from 0.4 to 6.4. Solid lines indicate the trends from experimental data and dash lines indicate values that we calculate using the relations in Equations (1) and (5). b) Plot showing figure of merit as a function of ion-beam current for a constant value of $\mathcal{S}$ = 1.6 and values of ζ ranging from 0.1 to 10.0. Solid lines indicate the trends from experimental data and dash lines indicate values that we calculate using the relation in Equations (1) and (5).

Note S10. Design of Fresnel lenses

A plane wave of incident light along the optical axis has a constant phase over the lateral extent of a spherical lens.[19] As a result of diffraction through the lens, the converging wave has the phase retardation distribution,

$$\psi(r) = \frac{2\pi}{\lambda}\left(f - \sqrt{f^2 - r^2}\right). \tag{S31}$$

where r is the radial position orthogonal to the optical axis, f is the focal length of the lens, and λ is the wavelength. Fresnel lenses with blazing exploit a sawtooth profile to modify $\psi(r)$ with a modulo 2π phase structure,

$$\psi_{\mathrm{F}}(r) = \psi(r) + 2m\pi, \tag{S32}$$

for $r_m < r \leq r_{m+1}$ where $r_m = \sqrt{2m\lambda f + (m\lambda)^2}$ is the inner radius of the zone radii.

The phase shift in the converging wave results from differences in the relative optical path length along the lens profile. In the design process, the phase retardation distribution determines the thickness of the Fresnel lens,

$$T(r) = \frac{\lambda}{\Delta n}\left[\frac{\psi_{\mathrm{F}}(r)}{2} + 1\right]. \tag{S33}$$

Fresnel lenses of this design have a numerical aperture of,

$$\mathrm{NA} = \frac{1}{\sqrt{1+\left(\frac{f}{R}\right)^2}} = \sin\theta. \tag{S34}$$

The Rayleigh criterion is,

$$d = 0.61\frac{\lambda}{\mathrm{NA}}. \tag{S35}$$

Note S11. Dose trimming

Tests of dose delivery are generally necessary in nanofabrication, and optimization methods can be either computational[15b] or empirical.[20] Our simple model of the bilayer response provides useful insights but ignores many details of the milling process, which would be desirable to account for in a computational optimization of dose delivery. At this state of the art, we develop an empirical method of dose optimization to minimize the differences between design and actual structure. This method involves trimming the ion dose near regions of high negative curvature to improve the masking of features that are sensitive to unintentional ion bombardment. Regions with high aspect ratios and extrema of negative curvature such as pillars, ridges, or blaze peaks are susceptible to such unintentional damage, which is likely to occur if actual and theoretical models of ion-beam profile deviate significantly or if dependences of milling rates on incidence angle are unknown. Reducing the ion dose in regions where the design of the surface specifies a curvature that exceeds a certain threshold can compensate for such discrepancies. The curvature of an axially symmetric surface, $z(r)$, is

$$\kappa(r) = \frac{z''}{(1 + z'^2)^{\frac{3}{2}}}, \tag{S36}$$

where $z' = \frac{\partial z(r)}{\partial r}$ and $z'' = \frac{\partial^2 z(r)}{\partial r^2}$ respectively denote the first and second derivatives of $z(r)$ with respect to r. A natural choice for a curvature threshold is the inverse of the lateral extent of the ion-beam profile, which we select to be a value of $-(4\sigma)^{-1}$, corresponding to the maximum negative curvature from the 95% coverage interval of a Gaussian approximation. Figure S18 shows the best result of three tests of trimming the ion dose around the blaze peaks in the milling of a Fresnel lens through chromia and into silica with an ion-beam current of 2600 pA.

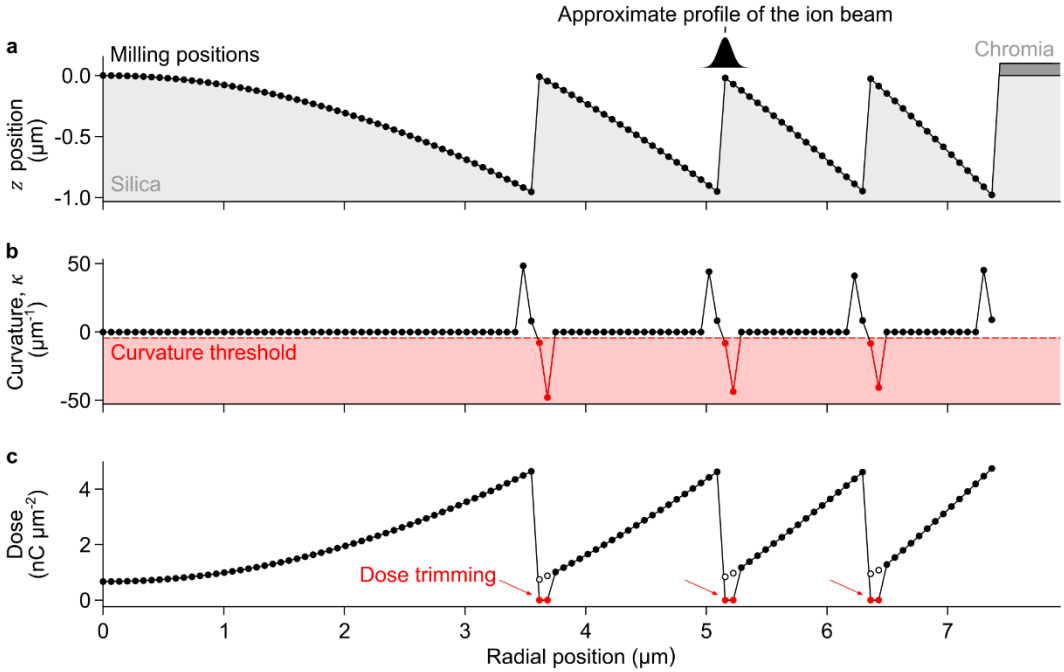

Figure S18. Dose trimming. a) Plot showing the radial profile of the design of a Fresnel lens, showing (black circles and solid black line) milling positions and (inset) an approximate profile of a Gaussian ion beam. b) Plot showing the curvature of the profile in (a) and (red dash line) a curvature threshold of $-(4\sigma)^{-1}$. c) Plot showing the radial dose profile resulting from trimming the ion dose at (white circles) milling positions that drop below the curvature threshold.

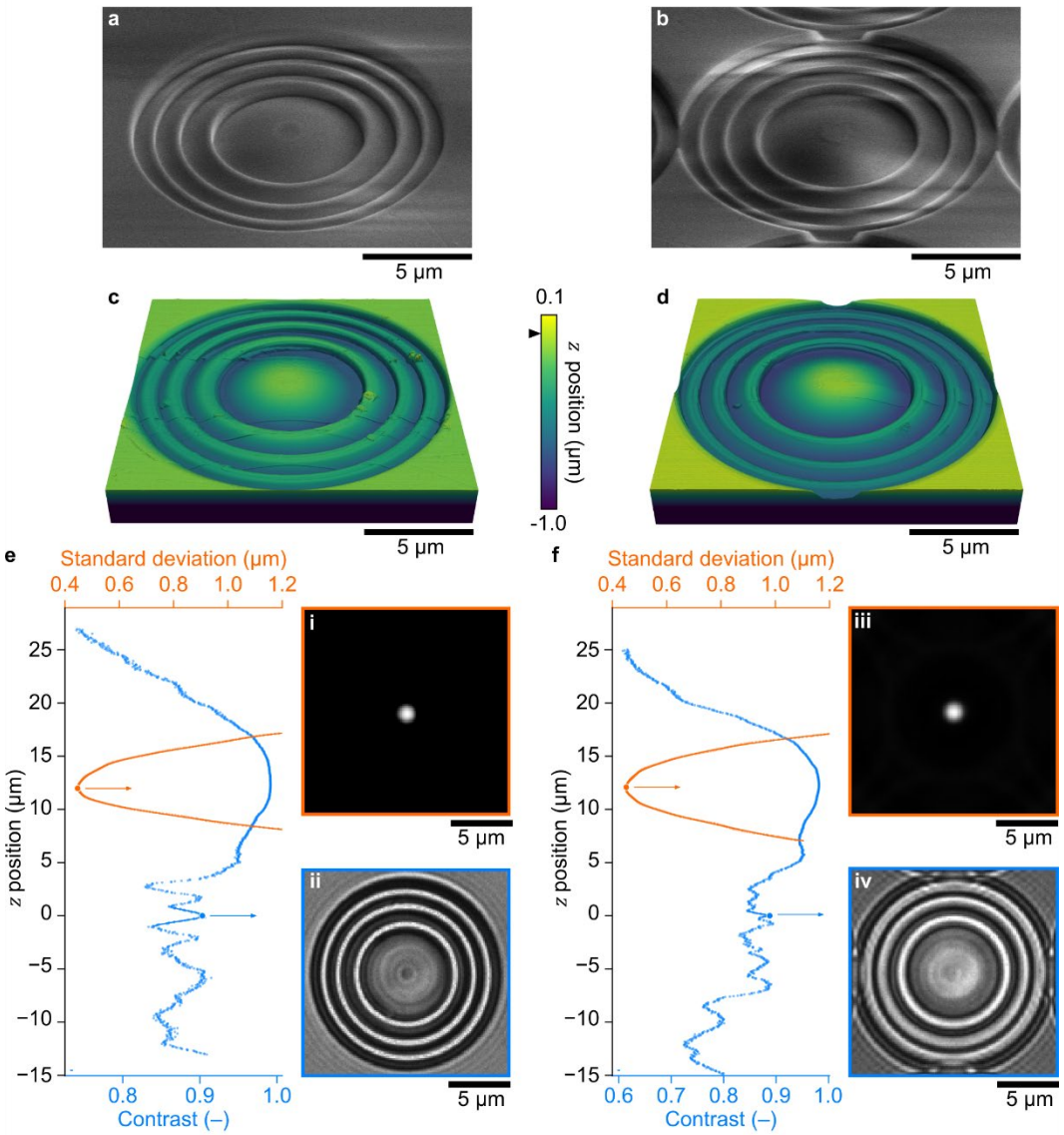

Figure S19. Fresnel lens characterization. a) and b) Scanning electron micrographs at a tilt angle of 0.9075 rad (52°) showing Fresnel lenses. c) and d) Atomic force micrographs at the same tilt angle showing the same Fresnel lenses in (a) and (b). e) and f) Plots showing (blue) contrast and (orange) standard deviation of Gaussian model fits to focal spot images from Fresnel lenses as functions of z position. (i-iv) Brightfield optical micrographs showing (i,iii) focal spots and (ii,iv) top surfaces of Fresnel lenses. Panels (a,c,e) correspond to Fresnel lenses that we mill directly into silica with an ion-beam current of 26 pA. Panels (b,d,f) correspond to Fresnel lenses that we mill through chromia and into silica with an ion-beam current of 2600 pA. Artifacts from charging are apparent in (a) and (b). Convolution artifacts of the probe tip are apparent in (c) and (d). The black triangle in (c,d) indicates the zero plane in both atomic-force micrographs and brightfield optical micrographs. Root-mean-square values of surface roughness in the central regions of either lens are approximatly 4 nm. Differences in contrast between (e-ii) and (f-iv) are partially attributable to diffraction effects from multiple lenses in close proximity in (f-iv). Lone blue bars in (e) and (f) indicate representative uncertainties of contrast as 95% coverage intervals. Uncertainties of standard deviation and *z* position from measurement repeatability are smaller than the data markers.

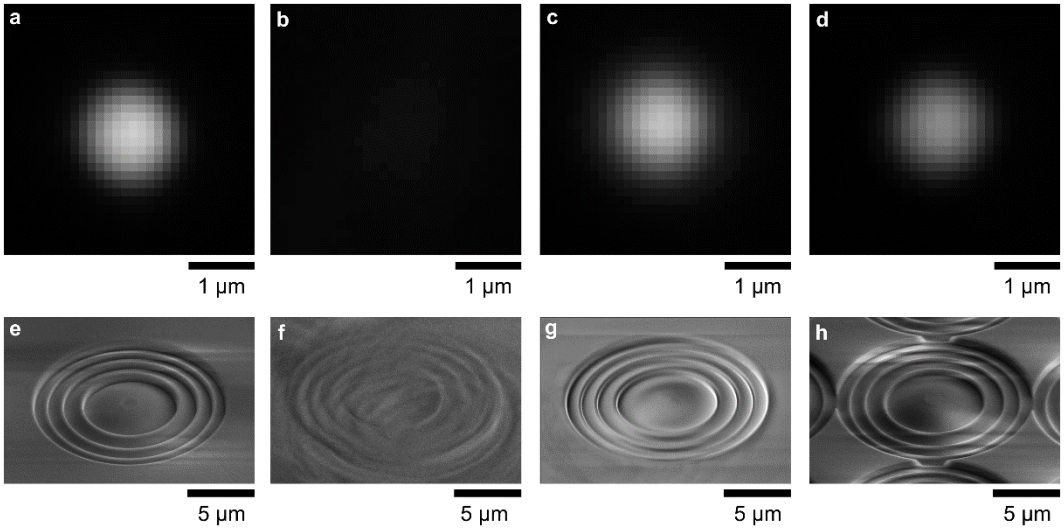

Figure S20. Fresnel lens comparison. a-d) Brightfield optical micrographs showing focal spots from Fresnel lenses that we machine under a variety of conditions (Table S14). e-h) Scanning electron micrographs showing the Fresnel lenses that project the focal spots in (a-d). Machining defects from charge accumulation extend beyond the region of interest in (f).

Table S14. Fresnel lens parameters

Material system	Ion-beam current (pA)	FWHM of ion beam (nm)	Electron-beam current (pA)	Number of lenses (–)	Milling time (h)	Lenses per hour (–)	Projection distance (µm)	Apparent standard deviation of focal spot (nm)	Data location (–)
Silica	26	14	100	1	3.75	0.27	11.97 ± 0.01	440.3 ± 0.1	Fig. S20 a,e
Silica	2600	133	0	1	0.04	25	–	–	Fig. S20 b,f
Silica	2600	133	6400	1	0.04	25	12.38 ± 0.40	503.6 ± 0.1	Fig. S20 c,g
Chromia on silica	2600	133	0	75	3.75	20	11.98 ± 0.19	439.1 ± 3.9	Fig. S20 d,h

FWHM = full width at half maximum
95% coverage intervals for the single lens in silica are measurement uncertainty.
95% coverage intervals for the 75 lenses through chromia in silica are measurement uncertainty and fabrication variability.
Uncertainties in this table are from measurement repeatibility only, neglecting systematic effects such as actuator non-linearity and image scale uncertainty. We make the approximation that these systematic effects cancel in a calculation of ratios of distances and standard deviations to determine relative differences with corresponding uncertainties.

References

[1] a) H. Janssen, *Reliability Engineering & System Safety* **2013**, 109, 123; b) T. Lafarge, A. Possolo, *NCSLI Measure* **2015**, 10, 20.
[2] K.-T. Liao, J. Schumacher, H. J. Lezec, S. M. Stavis, *Lab on a Chip* **2018**, 18, 139.
[3] a) J. S. Villarrubia, *Journal of Research of the National Institute of Standards and Technology* **1997**, 102, 425; b) P. Klapetek, I. Ohlídal, *Ultramicroscopy* **2003**, 94, 19.
[4] J. S. Villarrubia, A. E. Vladár, M. T. Postek, *Surface and Interface Analysis* **2005**, 37, 951.
[5] M. Yasaka, *The Rigaku Journal* **2010**, 26.
[6] C. R. Copeland, J. Geist, C. D. McGray, V. A. Aksyuk, J. A. Liddle, B. R. Ilic, S. M. Stavis, *Light: Science & Applications* **2018**, 7, 31.
[7] a) A. Possolo, National Institute of Standards and Technology, United States Department of Commerce, 2015; b) B. N. Taylor, C. E. Kuyatt, National Institute of Standards and Technology, United States Department of Commerce, 1994.
[8] N. Vladov, J. Segal, S. Ratchev, *Journal of Vacuum Science & Technology B* **2015**, 33, 041803.
[9] a) L. Reimer, *Scanning Electron Microscopy: Physics of Image Formation and Microanalysis*, Springer-Verlag Berlin Heidelberg, **1985**; b) J. S. Villarrubia, R. G. Dixson, A. E. Vladár, presented at Proceedings of SPIE **2010**.
[10] a) A. Vladár, J. Villarrubia, J. Chawla, B. Ming, J. Kline, S. List, M. Postek, presented at Proceedings of SPIE **2014**; b) J. S. Villarrubia, A. E. Vladár, B. Ming, R. J. Kline, D. F. Sunday, J. S. Chawla, S. List, *Ultramicroscopy* **2015**, 154, 15.
[11] D. Izraelevits, *Photogrammetric Engineering & Remote Sensing* **2003**, 69, 767.
[12] A. Savitzky, M. J. E. Golay, *Analytical Chemistry* **1964**, 36, 1627.

[13] a) B. Efron, C. Stein, *Annals of Statistics* **1981**, 9, 586; b) M. H. Quenouille, *Annals of Mathematical Statistics* **1949**, 20, 355.
[14] T. Matsuyama, *Advanced Powder Technology* **2019**, 30, 2616.
[15] a) G. B. Assayag, C. Vieu, J. Gierak, P. Sudraud, A. Corbin, *Journal of Vacuum Science & Technology B* **1993**, 11, 2420; b) J. Han, H. Lee, B.-K. Min, S. J. Lee, *Microelectronic Engineering* **2010**, 87, 1.
[16] N. I. Borgardt, A. V. Rumyantsev, *Journal of Vacuum Science & Technology B* **2016**, 34, 061803.
[17] L. D. Menard, J. M. Ramsey, *Nano Letters* **2011**, 11, 512.
[18] N. S. Smith, W. P. Skoczylas, S. M. Kellogg, D. E. Kinion, P. P. Tesch, O. Sutherland, A. Aanesland, R. W. Boswell, *Journal of Vacuum Science & Technology B* **2006**, 24, 2902.
[19] H. Nishihara, T. Suhara, in *Progress in Optics*, Vol. 24 (Ed: E. Wolf), Elsevier **1987**, p. 1.
[20] H. Lee, J. Han, B.-K. Min, S. J. Lee, *Applied Physics Express* **2008**, 1, 127002.